



City Research Online

City St George's, University of London

Citation: Deng, X-F., Shilin, L., Fu, F. & Qian, K. (2020). Effects of High Strength Concrete on Progressive Collapse Resistance of Reinforced Concrete Frame. *Journal of Structural Engineering*, 146(6), 04020078. doi: 10.1061/(asce)st.1943-541x.0002628

This is the accepted version of the paper.

This version of the publication may differ from the final published version. To cite this item please consult the publisher's version.

Permanent repository link: <https://openaccess.city.ac.uk/id/eprint/23075/>

Link to published version: [https://doi.org/10.1061/\(asce\)st.1943-541x.0002628](https://doi.org/10.1061/(asce)st.1943-541x.0002628)

Copyright and Reuse: Copyright and Moral Rights remain with the author(s) and/or copyright holders. Copies of full items can be used for personal research or study, educational, or not-for-profit purposes without prior permission or charge, unless otherwise indicated, provided that the authors, title and full bibliographic details are credited, a hyperlink and/or URL is given for the original metadata page and the content is not changed in any way. For full details of reuse please refer to [City Research Online policy](#).

Effects of High Strength Concrete on Progressive Collapse Resistance of Reinforced Concrete Frame

Xiao-Fang Deng¹, Shi-Lin Liang², Feng Fu³, C.Eng, M.ASCE and Kai Qian⁴ Ph.D, M.ASCE

ABSTRACT

The application of extreme loads such as impact and blast may lead to progressive collapse and the robustness of a structure must be considered in this context. Although extensive studies had been carried out over the past decades to study the load resisting mechanism of reinforced concrete (RC) frames to prevent progressive collapse, the effects of high-strength-concrete (HSC) on progressive collapse resistance capacity is still unclear. Therefore, six tests of RC frames with different span-to-depth ratio and concrete strength were conducted in present study. Among them, three are HSC frames and the remaining are normal strength concrete frames. It was found that the use of HSC could further enhance the compressive arch action (CAA) capacity, especially for those with low span-to-depth ratio. On the other hand, HSC can reduce the tensile catenary action (TCA) capacity at large deformation stage, primarily because of higher bond stress between concrete and rebar, leading to earlier fracture of the rebar. The analytical results from the model were compared with the test results. It was found that the refined CAA model could accurately predict the CAA capacity of NSC frames, but not for HSC frames. Moreover, existing model is hard to predict the CAA capacity of the frames with relatively small span-to-depth ratio (less than 7) accurately.

CE Database subject heading: progressive collapse; high strength concrete; compressive arch action; tensile catenary action

¹ Assistant Professor in College of Civil Engineering and Architecture at Guangxi University, China, 530004, xiaofang.deng@gxu.edu.cn

² Research Student in College of Civil Engineering and Architecture at Guangxi University, China, 530004, liangshilin@st.gxu.edu.cn

27 ³ Senior Lecturer in Structural Engineering, School of Mathematics, Computer Science and Engineering, City, University
28 of London, U.K., Feng.Fu.1@city.ac.uk
29 ⁴Professor in College of Civil Engineering and Architecture at Guangxi University, China, 530004, (corresponding author)
30 qiankai@gxu.edu.cn
31

32 **INTRODUCTION**

33 Buildings may subject to initial local damage due to intended or accidental events, such as the loss of
34 one or a couple of columns. However, in ordinary civilian building design, the column missing is not
35 well considered in the past design guidelines. Therefore, these buildings may have high risk to
36 propagate initial local damage disproportionately to a large area of the building or even cause entire
37 collapse. The terminology of progressive collapse is first proposed after the collapse of Ronan Point in
38 1968. The collapse of Murrah Federal Building in 1995 and Twin-Tower of World Trade Center in
39 2001 re-sparked the interest on progressive collapse in academic and practical engineer's communities.
40 Several design codes or guidelines (BS8110 1997; BSI 2006; GSA 2009; ASCE/SEI 7 2010; DoD
41 2009; ACI-318 2014) were issued for progressive collapse design using so-called explicitly or
42 implicitly design methods. Among them, Alternate Load Path method is commonly accepted for
43 evaluation of the capacity of a building to mitigate progressive collapse due to its threat independent
44 feature.

45 Based on Alternate Load Path method, extensive tests had been carried out in the past decades to
46 understand the capacity of reinforced concrete (RC) frames to resist progressive collapse. These tests
47 could be categorized into three groups: multi-story tests (Yi et al. 2008; Sasani et al. 2011a; Xiao et al.
48 2015; Qian and Li 2017; Qian et al. 2019), single-story beam-column or beam-column-slab
49 subassembly tests (Su et al. 2009; Orton et al. 2009; Qian and Li 2012a; FarhangVesali et al. 2013; Yu
50 and Tan 2013a; Lew et al. 2014; Valipour et al. 2015a; Qian et al. 2016; Ren et al. 2016; Peng et al.
51 2017; Qian et al. 2018), and single-story beam-column connections tests (Qian and Li 2012b; Yu et al.
52 2014). Yi et al. (2008) carried out a 1/3-scaled three-story planar frame test to evaluate the load
53 resisting mechanism of RC frame subjected to the loss of an interior column. Compressive arch action
54 (CAA) and tensile catenary action (TCA) were found to be the primary mechanisms in resisting

55 progressive collapse at different stages. Sasani et al. (2011a) conducted a real time removal test to
56 study the dynamic response of an 11-story building, which was planned to be demolished, subjected to
57 sudden removal of four adjacent ground columns due to explosives. Flexural beam action and
58 Vierendeel action were identified as the two primary load resisting mechanisms. Xiao et al. (2015)
59 experimentally investigated the dynamic response of a half-scaled three-story RC building, which is
60 deliberately built for progressive collapse study, subjected to different column missing scenarios. The
61 load resisting mechanism shifted from flexural moment resisting to TCA mechanism was observed
62 when two ground exterior columns were removed simultaneously. Qian and Li (2017) tested a series of
63 six three-story frames with or without infilled walls to quantify the effects of masonry infilled walls on
64 load resisting mechanism and capacity of RC frames to resist progressive collapse. It was found that
65 masonry infilled walls enhance the initial stiffness and increase the first peak load significantly.
66 Moreover, the crushing of masonry infilled walls will not jeopardize the development of TCA of the
67 beam at large deformation stage. Qian et al. (2019) also tested another series of five three-story frames
68 to quantify the efficiency of using steel bracings in strengthening RC frames to mitigate progressive
69 collapse. Different configurations of steel bracings were applied. It was found that compressive
70 bracings prone to out-of-plane buckling and have little contribution to the collapse resistance, while
71 tensile bracings may fracture before the development of TCA.

72 Actually, majority of existing tests on progressive collapse investigation were focused on beam-
73 column substructures or beam-column-slab substructures. This is because it is easier to replicate the
74 boundary conditions and measure the response. Dynamic effects and dynamic load increase factor of
75 RC frames subjected to sudden column removal scenario were also investigated (Qian and Li 2012b;
76 Yu et al. 2014; Peng et al. 2017). These literatures documented that the failure mode and resistance of
77 the specimens were similar to their counterparts tested in a static test manner. Moreover, the behavior
78 of beam-column connections subjected to different column missing scenarios were evaluated
79 experimentally by Yap and Li (2011) and Qian and Li (2012c), which could provide sufficient
80 evidence for the level of confidence in simplification of the boundary conditions in substructure tests.

81 The load resisting mechanisms of bare RC frames subjected to middle column missing scenario
82 were quantified by pushdown test methods (Su et al. 2009; FarhangVesali et al. 2013; Valipour et al.
83 2015a). Su et al. (2009) concluded that loading rate has little effect on CAA capacity. FarhangVesali et
84 al. (2013) reported that longitudinal reinforcement ratio and stirrup configuration have a minor effect
85 on the CAA. Valipour et al. (2015a) experimentally investigated the effects of concrete strength
86 (ranging from 18 MPa to 67 MPa) on the CAA of RC beam assemblages. The test results demonstrated
87 that the concrete strength has significant influence on the peak load capacity (CAA capacity) of the
88 tested specimens. The stiffness of supports also has significant effects on mobilization of CAA.
89 Valipour et al. (2015b) filled knowledge gap in progressive collapse response of RC frame using steel
90 fiber to replace conventional transverse reinforcements, the test results demonstrated that the
91 replacement had little effects on the development of TCA. The role of slabs, compressive membrane
92 action (CMA) and tensile membrane action (TMA) developed in RC slabs were evaluated (Qian and
93 Li 2012a; Qian et al. 2016; Ren et al. 2016). It was found that, the CMA and TMA bring great benefit
94 to the resistance. The CMA capacity was affected by the stiffness of boundary elements and strength
95 of concrete significantly while the TMA capacity was mainly affected by the amount of slab
96 reinforcement in bottom layer (continual). Moreover, improving CMA of precast concrete slabs to
97 resist wheel loading using additional transverse confining system (i.e., straps, cross-bracing and a
98 combination of straps and cross-bracing) was reported by Valipour et al. (2015c). It was found that the
99 peak load capacity could be enhanced significantly due to considerable restraint provided by the
100 confining system. Furthermore, the effects of seismic design and detailing on behavior of RC moment
101 frames to resist progressive collapse were evaluated (Choi and Kim 2011, Qian and Li 2012c, Kim and
102 Choi 2016, Lu et al. 2017). Choi and Kim (2011) and Kim and Choi (2016) indicated that seismically
103 designed specimens performed much better than the corresponding non-seismically designed
104 specimens as seismically designed specimens had higher reinforcement ratio and transverse
105 reinforcement installed at joint zones, which delayed the failure of exterior joints. Lu et al. (2017)
106 found that for normal strength concrete frames, seismically design could increase the beam

107 longitudinal reinforcement ratio, which resulted in a much larger resistance in both beam and catenary
108 action. However, the increase of beam depth could improve the resistance of beam action but not the
109 catenary action. Moreover, the results from Kim et al. (2011) indicated that rotational friction damper,
110 which was normally for mitigating seismic or wind load, was also effectively improve the behavior of
111 RC frames to mitigate progressive collapse.

112 Although above studies had deeply improved the understanding on load resisting mechanisms of
113 RC frames to resist progressive collapse, these studies are mainly focused on normal strength concrete
114 (NSC). As high strength concrete (HSC) has advantages in load resisting capacity enhancement,
115 smaller member size, less self-weight etc, HSC is widely used in high-rise buildings in the past
116 decades. Moreover, the high-rise buildings have higher possibility for terrorism attacks due to their
117 higher social impact caused by attacks. Thus, it is necessary to evaluate the behavior of reinforced
118 HSC frames to resist progressive collapse and to identify the effects of HSC on load resisting
119 mechanism of RC frames. For this purpose, a series of six RC frames, using both HSC and NSC, were
120 designed and tested under pushdown loading regime. The accuracy of existing analytical models in
121 predicting CAA and TCA of HSC frames was also evaluated.

122 **DESCRIPTION OF TEST PROGRAM**

123 **Experimental specimens**

124 Six half-scaled beam-column sub-assemblages were designed and constructed to evaluate the effects of
125 HSC on behavior of RC frames to resist progressive collapse. These specimens include three HSC
126 specimens (HSC-13, HSC-11, and HSC-8) and three NSC specimens (NSC-13, NSC-11, and NSC-8).
127 The specimens are denoted flows below conventions:

- 128 1. 'HSC' represents specimens using HSC and 'NSC' represents specimens using NSC;
- 129 2. Number after hyphen denotes span/depth ratio, which is defined by the ratio of clear beam span
130 to its depth.

131 Fig. 1 shows the dimension and reinforcement details of specimen NSC-11 while Table 1 lists the key
132 properties of the specimens. As shown in Fig. 1, Specimen NSC-11 was non-seismically designed in
133 accordance with ACI 318-14 (2014) with clear span of 2750 mm and beam cross-section of 250
134 mm×150 mm. The bottom rebar is continuous 2T12 reinforcement, while curtailment is considered for
135 top rebar. The beam transverse reinforcement is R6@100 mm throughout the whole beam without
136 transverse reinforcements in the joint zone. The clear cover of the concrete for beam and column are
137 both 15 mm. T12 and R6 herein represent deformed reinforcement with diameter of 12 mm and plain
138 reinforcement with diameter of 6 mm, respectively. Two beams, one middle column stub, and two
139 enlarged side column stubs were casted. The enlarged side column has dimension of 400 mm×400 mm
140 to replicate fixed boundary conditions following previous studies (Orton et al. 2009; Su et al. 2009; Yu
141 and Tan 2013a).

142 As tabulated in Table 1, Specimens NSC-13 and NSC-8 have similar reinforcement ratio and
143 beam cross-section to Specimen NSC-11 but clear span of 3250 mm and 2000 mm, respectively.
144 Specimens HSC-13, HSC-11, and HSC-8 have identical dimensions and reinforcement details to NSC
145 counterparts but high strength concrete is used. According to cylindrical compression tests, at the day
146 of test, the recorded concrete compressive strength of NSC-13, NSC-11, NSC-8, HSC-13, HSC-11,
147 and HSC-8 are 30.5 MPa, 31.1 MPa, and 31.7 MPa, 59.3 MPa, 61.2 MPa, and 60.5 MPa, respectively.
148 Based on tensile splitting tests, the tensile strength of the concrete of NSC-13, NSC-11, NSC-8, HSC-
149 13, HSC-11, and HSC-8 are 2.9 MPa, 3.0 MPa, 2.9 MPa, 6.0 MPa, 6.1 MPa, and 6.1 MPa, respectively.
150 Moreover, the properties of reinforcement are tabulated in Table 2.

151 **Test Setup and instrumentations**

152 Similar to previous studies (Orton et al. 2009; Su et al. 2009; Yu and Tan 2013a), as shown in Fig. 2a,
153 fixed boundary condition was replicated at the side column by using two rollers and one bottom pin.
154 To eliminate the redundant horizontal restraints from the bottom pin, a series of steel rollers were
155 placed below the pin support. Therefore, the side columns were statically determinate and the

156 horizontal and vertical reaction force could be measured directly. It is intentionally designed with no
157 middle column at ground level due to desired element removal before applying vertical load. The
158 column removal effect is implemented through a hydraulic jack with a downward stroke of 700 mm.
159 Displacement-controlled method was adopted with a rate of 0.5 mm/s throughout the tests. To prevent
160 out-of-plane failure, a specially designed steel assembly was installed below the hydraulic jack. As
161 illustrated in Fig. 2b, two load cells were installed above and below the hydraulic jack to measure the
162 vertical load (average value was used for final test results records hereafter). In addition, load cell was
163 installed below each pin support to monitor the load redistribution of the columns.
164 Tension/compression load cell (Item 5 in Fig. 2b) was installed in each horizontal roller to measure the
165 horizontal reaction force. A series of linear variable displacement transducers (LVDTs) were installed
166 along the beam (D1 to D7) to monitor the deformation shape during test. LVDTs (H1 and H2) were
167 also installed horizontally at the side columns to determine the stiffness of the horizontal restraints as
168 gap allowance was inevitable when installation of the appliance. Strain gauges were mounted along the
169 length of beam longitudinal reinforcements before casting.

170 **EXPERIMENTAL RESULTS**

171 **General behavior**

172 **NSC-series:** Fig. 3a shows the vertical load-displacement curve of NSC-series specimens and Fig.
173 4a shows the development of crack pattern of NSC-11. For NSC-11, first crack occurred at the beam
174 ends when the middle joint displacement (MJD) reached 9 mm. When the MJD reached 36 mm, the
175 yield load of 37 kN was obtained. However, the calculated yield strength due to pure bending
176 resistance was 35 kN, which was less than the measured one. This was mainly because of the inherent
177 compressive axial force in reality is not taken into consideration in the analytical model. Further
178 increasing the MJD, the CAA capacity of 52 kN was observed at an MJD of 90 mm, which is called
179 peak displacement in this study. As shown in Fig. 4a, at this loading stage, concrete crushing was
180 observed at the beam ends. The ratio of CAA capacity to yield load is about 1.41, which is due to

181 strain hardening of reinforcements and the mobilization of CAA. After that, the load resistance began
182 to drop gradually due to concrete crushing and second-order effects. However, the load resistance
183 began to re-ascend when the MJD reached 288 mm (about $0.1l_n$) due to the start of TCA. As shown in
184 Fig. 4a, penetrated cracks occurred at this stage. Further increasing displacement, more penetrated
185 cracks were observed which were uniformly distributed along the beam length. The drop of load
186 resistance was due to fracture of bottom rebar in the region of the beam-middle column interface. The
187 TCA capacity of 94 kN was obtained at an MJD of 712 mm. After that, the load resistance suddenly
188 dropped significantly because the complete fracture of the top rebar near the beam-middle column
189 joint. Fig. 5 shows the failure mode of NSC-11. As shown in the figure, severe concrete crushing
190 occurred at the beam ends while rebar fracture occurred primarily at beam end near middle joint region.
191 Penetrated cracks were uniformly distributed along the beam.

192 For NSC-13 and NSC-8, similar crack pattern and global behavior were observed. The yield load
193 of NSC-13 and NSC-8 was 33 kN and 53 kN, respectively. The calculated yield load of NSC-13 and
194 NSC-8 was 30 kN and 48 kN, respectively based on the analytical model. Similarly, the calculated
195 yield load is less than the measured one, which is primarily due to ignorance of compressive axial
196 force. For NSC-13, the CAA capacity of 43 kN was measured at an MJD of 108 mm. However, for
197 NSC-8, the CAA capacity was 77 kN, which was about 179 % and 148 % of that of NSC-13 and NSC-
198 11, respectively. Moreover, the TCA capacity of NSC-13 and NSC-8 was 81 kN and 88 kN,
199 respectively whereas the deformation capacity of NSC-13 and NSC-8 was 731 mm and 581 mm,
200 respectively. Although the TCA capacity of NSC-13 was less than that of NSC-11 and similar
201 deformation capacity was measured for them as shown in Fig. 3a. The test of NSC-13 was forced to
202 stop due to limited stroke capacity of the jack, rather than the failure of the specimen. If the jack had
203 larger stroke capacity, the deformation capacity and TCA capacity of NSC-13 would have been larger.
204 Figs. 6 and 7 show the failure modes of NSC-13 and NSC-8. In general, the failure mode of NSC-13
205 was similar to that of NSC-11. However, different to NSC-11 and NSC-13, the diagonal shear cracks

206 along the beams of NSC-8 were observed, rather than flexural cracks perpendicular to the beam axis.
207 This indicated the shear failure in this test.

208 **HSC-series:** Fig. 3b shows the vertical load-middle joint displacement curve of HSC-series
209 specimens. For HSC-11, first cracks occurred at the beam ends when the MJD reached 15 mm. At an
210 MJD of 28 mm, yield load of 42 kN, which was 114 % of that of NSC-11, was obtained. Further
211 increasing MJD to 74 mm, the CAA capacity of 60 kN, which was 115 % of that of NSC-11, was
212 achieved. The TCA capacity and deformation capacity of HSC-11 were 80 kN and 663 mm
213 respectively, less than these of NSC-11. The smaller deformation capacity in HSC-11 is mainly due to
214 high strength concrete resulted in high bond strength between reinforcement and concrete, which led to
215 stress concentration and rebar fracture in the tests. Fig. 4b shows the crack pattern of HSC-11.
216 Compared to NSC-11, it can be found that the high strength concrete has little effects on crack
217 development. The failure mode of HSC-11 is shown in Fig. 8, which is similar to that of NSC-11. As
218 shown in Fig. 3b and Table 3, due to larger span/depth ratio, HSC-13 only achieved yield load and
219 CAA capacity about 86 % and 80 % of these of HSC-11. Similar to normal strength concrete, HSC-13
220 experienced larger deformation. The lower TCA capacity of HSC-13 was caused by the insufficient
221 stroke capacity during the tests. On the contrast, for HSC-8, its yield load capacity and CAA capacity
222 were 133 % and 152 % of these of HSC-11. Different to rest specimens, the TCA capacity of HSC-8 is
223 less than its CAA capacity, which will be further discussed in analytical section of this paper. The
224 failure mode of HSC-13 and HSC-8 are illustrated in Figs. 9 and 10, respectively. For HSC-13, only
225 bottom rebar near the middle joint were fractured. For HSC-8, both bottom and top rebar near the
226 middle joint were fractured.

227 **Horizontal reaction**

228 The horizontal reaction force v.s. middle joint displacement curves are shown in Fig. 11. As shown in
229 Fig. 11a, the horizontal compressive force increased with the increase of vertical displacement. For
230 NSC-11, the horizontal compressive force was -70 kN at yield displacement, which explains the reason

231 that the calculated yield load is less than the measured one. The maximum horizontal compressive
232 force was -178 kN at an MJD of 180 mm, which was greater than the corresponding peak displacement.
233 Then, the horizontal compressive force began to decline with further increase of the displacement. The
234 horizontal compressive force transferred to horizontal tensile force after the MJD of 356 mm. The
235 maximum horizontal tensile force of 154 kN was measured at the MJD of 699 mm. Similar behavior
236 was observed for NSC-13 and NSC-8. The maximum horizontal compressive force of NSC-13 and
237 NSC-8 were -153 kN and -202 kN, respectively. Thus, when span/depth ratio reduced from 11 to 8, the
238 maximum horizontal compressive force increased by 13.4 %. Conversely, increasing the span/depth
239 ratio from 11 to 13, the maximum horizontal compressive force decreased by over 14.0 %. Moreover,
240 the maximum horizontal tensile force of NSC-13 and NSC-8 were 148 kN and 147 kN, respectively.
241 Thus, span/depth ratio will not affect the development of horizontal tensile force.

242 As shown in Fig. 11b, the maximum horizontal compressive force of HSC-11, HSC-13, and HSC-
243 8 were -259 kN, -233 kN, and -321 kN, respectively. Thus, when span/depth ratio decreased from 11
244 to 8, the maximum horizontal compressive force was increased by 23.9 %, which was greater than that
245 of the NSC specimens. For the maximum horizontal tensile force, similar to NSC specimens, the
246 span/depth ratio will not affect it significantly.

247 **Deflection shape of beams**

248 Fig. 12 shows the beam deflection shape of NSC-11 in accordance with different critical stages: yield
249 load capacity, CAA capacity, onset of TCA, fracture of rebar, and ultimate deformation. As shown in
250 the figure, from the beginning of the test, the beams exhibit double-curvature deflection shape. Before
251 fracture of the first rebar near the middle joint, the beams' deformation was almost symmetric. Then,
252 the middle joint continued to rotate and the damage prone to be concentrated in the left side of the
253 middle joint due to the weld failure between the top of the middle stub and the steel column, which
254 released the rotational restraints at the middle joint. Moreover, at the final stage of test, the chord
255 rotation, which is defined as ratio of MJD to beam span, was compared with the beam deformation

256 shape. It can be seen that the chord rotation will over-estimate the actual end rotation of the beam end
257 near the side columns while it could estimate the rotation of the beam end near the middle joint well.
258 For other specimens, similar results were observed.

259 **Strain gauge results**

260 Figs. 13a and b show the variation of strain gauge readings along beam top and bottom longitudinal
261 reinforcements of NSC-11, respectively. As shown in the figure, the bottom reinforcement near the
262 middle joint was first yielded. At CAA stage, plastic hinges were formed at both beam ends. However,
263 the compressive strain in both top and bottom rebar began to decline after onset of the TCA stage. At
264 ultimate load stage, no compressive strain was measured at both top and bottom beam longitudinal
265 reinforcement. As shown in Fig. 14, the strain variation of HSC-11 was quite similar to that of NSC-11.
266 However, as shown in Fig. 15, at ultimate load stage, considerable compressive strain was still
267 measured at bottom reinforcement of HSC-8. This could be explained as the high bond between
268 concrete and rebar as well as low span-depth ratio resulted in earlier fracture of longitudinal rebar and
269 delayed the development of tensile strain in rebar.

270 **ANALYSIS AND DISCUSSIONS**

271 **Dynamic response of tested specimens**

272 As progressive collapse is a dynamic event due to the sudden column removal, it was worthwhile to
273 evaluate the dynamic capacity of test specimens. Based on the investigation from Qian and Li (2015a,
274 b) and Tsai (2010), an energy-based simplified single-degree-of-freedom (SDOF) model, first
275 proposed by Izzuddin et al. (2008), is accurate for dynamic assessment. Thus, in this study, the energy-
276 based model was utilized to assess the dynamic capacity of specimens based on the measured quasi-
277 static load-displacement curves from the tests. The mathematic equations were expressed as:

$$278 \quad P_d(u_d) = \frac{1}{u_d} \int_0^{u_d} P_{NS}(u) du \quad (1)$$

279 where $P_d(u)$ and $P_{NS}(u)$ are the dynamic capacity and the nonlinear static loading estimated at the
280 displacement demand u , respectively.

281 Fig. 16 shows the dynamic response curves of tested specimens. As shown in the figure, the
282 dynamic ultimate capacity of NSC-13, HSC-13, NSC-11, HSC-11, NSC-8, and HSC-8 were 44 kN, 43
283 kN, 53 kN, 53 kN, 64 kN, and 78 kN, respectively. Thus, the higher strength concrete has little effects
284 on dynamic ultimate capacity of the specimens with moderate or large span/depth ratio. This is
285 primarily because TCA governs the failure. However, for specimens with small span/depth ratio, high
286 strength concrete could increase the dynamic ultimate capacity significantly as CAA governs the load.

287 **De-composition of the load resistance contribution from axial force and bending moment**

288 To de-composite the resistance contribution from the axial force and bending moments, a series of
289 analyses were carried out. As shown in Fig. 17, only left bay was extracted for analysis due to
290 symmetry. The load resistance P could be determined as the summation of the vertical components of
291 the shear force (V) and axial force (N) at the middle joint when the MJD was δ .

$$292 \quad P = (N \sin \theta + V \cos \theta) \quad (2)$$

293 where θ is the rotation of the beam end near the middle joint and can be determined by the vertical
294 displacements ($\theta = \arctan\left(\frac{4(D_4 - D_3)}{l}\right)$); D_3 is the vertical displacement measured at the position
295 with $l/4$ from the middle joint, and D_4 is the MJD; l is beam span length.

296 As shown in Fig. 17, N and V could be determined by the measured horizontal and vertical
297 reaction force at the supports:

$$298 \quad N = (F_L \tan \theta + H_t + H_b) \cos \theta \quad (3)$$

$$299 \quad V = (F_L - N \sin \theta) / \cos \theta \quad (4)$$

300 Therefore, the bending moment at the beam end near the middle column (M_M) and the one near
301 the side column (M_S) could be expressed as:

$$302 \quad M_M = F_L l - H_t(\delta + 0.35) - H_b(\delta - 0.35) \quad (5)$$

$$303 \quad M_S = 0.2F_L - 0.35H_t + 0.35H_b \quad (6)$$

304 where H_t and H_b are the horizontal reaction force at the upper roller and bottom roller, respectively; F_L
305 is the vertical reaction force at the left side column.

306 NSC-11, HSC-11, NSC-8 and HSC-8 were selected to show the de-composition of load resistance,
307 as shown in Fig. 18. As shown in the figure, initially the contribution from axial force is negative due
308 to development of compressive force at CAA stage. At this stage, the load resistance mainly attributed
309 to the shear force. When tensile force mobilized at TCA stage, the contribution of axial force increased
310 with increase of MJD. However, as shown in the figure, the contribution from shear force is still
311 significant although the contribution from shear force is decreasing with the increase of MJD. Thus, it
312 is not correct to assume the load resistance purely provided from tension force of reinforcement at
313 TCA stage.

314 Figs. 19a, b, c and d show the variation of bending moment of NSC-11, HSC-11, NSC-8 and
315 HSC-8, respectively. As shown in the figure, the bending moments were much larger than expected
316 pure flexural induced bending moments due to compressive force developed in the beams. Moreover,
317 the maximum bending moment and maximum compressive axial force achieved at the same MJD. For
318 NSC-11, the maximum bending moments near the middle column and near the side column were 46.7
319 kN·m and 48.7 kN·m, respectively. Compared with NSC-11, the maximum bending moments of HSC-
320 11 were increased by 36.2 % and 38.8 %, respectively. Similarly, compared to NSC-8, the bending
321 moment near the middle column and side column of HSC-8 were increased by 34.3 % and 12.2 %,
322 respectively.

323 The measured M-N curves of NSC-11, NSC-8, HSC-11, and HSC-8 were presented in Figs. 20,
 324 21, 22, and 23, respectively. It was found that the M-N curves were similar to the theoretical M-N
 325 curves for both NSC and HSC specimens. When the bending moment reached its maximum value, the
 326 bending moment began to decrease as the axial force changed from compression to tension at large
 327 deformation stage. As shown in the figure, even the axial force in tension (catenary action kicked in),
 328 the M-N curves agreed with the theoretical ones well.

329 Assessment of the accuracy of existing CAA models

330 As a favorable alternate load path to resist progressive collapse due to its low demand in
 331 deformation, CAA has been widely studied theoretically. Based on plastic theory, Park and Gamble
 332 (2000) proposed a classical model to calculate the CMA in RC slabs. The Park and Gamble (2000)'s
 333 model can be further used to predict CAA capacity in RC beam as the CMA and CAA share similar
 334 merits. As shown in Fig. 24, the CAA capacity P can be given as:

$$335 \quad P_{CAA} = \frac{2(M_s + M_m - N\delta)}{\beta L} \quad (7)$$

336 where M_s and M_m are the bending moments at the beam-column interface; N is the axis force in beam;
 337 L is the total span of the double-bay beam; β is the ratio of the net span to the total span L , which is 0.5
 338 here; δ is the vertical displacement in the middle column stub. After stringent derivation, which can be
 339 found in Park and Gamble (2000) in detail, P can be expressed as:

$$340 \quad P_{CAA} = \frac{2}{\beta L} \left\{ 0.85f_c' \beta_1 h b \left[\frac{h}{2} \left(1 - \frac{\beta_1}{2} \right) + \frac{\delta}{4} (\beta_1 - 3) + \frac{\beta L^2}{4\delta} (\beta_1 - 1) \left(\varepsilon + \frac{2t}{L} \right) \right. \right. \\
 + \frac{\delta^2}{8h} \left(2 - \frac{\beta_1}{2} \right) + \frac{\beta L^2}{4h} \left(1 - \frac{\beta_1}{2} \right) \left(\varepsilon + \frac{2t}{L} \right) - \frac{\beta_1 \beta^2 L^4}{16h\delta^2} \left(\varepsilon + \frac{2t}{L} \right)^2 \left. \right] \\
 - \frac{1}{3.4f_c'} (T_s - T_m - T_s' + T_m')^2 + (T_s' + T_m') \left(\frac{h}{2} - a_s - \frac{\delta}{2} \right) \\
 + (T_s + T_m) \left(h_0 - \frac{h}{2} + \frac{\delta}{2} \right) \left. \right\} \quad (8)$$

341 and

$$\varepsilon + \frac{2t}{L} = \frac{\left(\frac{1}{hE_c b} + \frac{2}{LK}\right) \left[0.85 f_c' \beta_1 b \left(\frac{h}{2} - \frac{\delta}{4} - \frac{T_s - T_m - T_s' + T_m'}{1.7 f_c' \beta_1 b} \right) + T_m' - T_m \right]}{1 + 0.2125 \frac{f_c' \beta_1 \beta L^2 b}{\delta} \left(\frac{1}{hE_c b} + \frac{2}{LK} \right)} \quad (9)$$

where h and b are the beam depth and beam width, respectively; β_1 is the ratio of the depth of the concrete equivalent rectangular stress block to the depth of neutral-axis; ε is the axial strain of the double-bay beam; t is the axial movement of the side column stub; T_s and T_m are the steel tensile forces at side beam-column interface and middle beam-column interface, respectively; T_s' and T_m' are the steel compressive forces at side beam-column interface and middle beam-column interface, respectively; f_c' is the concrete cylinder compression strength; h_0 is the effective depth of the beam; a_s is the distance from the centroid of compressive steel to the concrete compression surface; E_c is the concrete elastic modulus; K is the lateral stiffness.

To evaluate the accuracy of the model, 45 specimens from existing tests (Su et al.2009, Choi and Kim 2011, Sasani et al. 2011b, FarhangVesali et al. 2013, Valipour et al. 2015a, Yu and Tan 2013b, Yu and Tan 2014, Qian et al. 2015, Alogla et al. 2016, Ren et al. 2016) were used for assessment. Table 4 presents the key parameters and analytical results. As shown in Fig. 25a, the mean value and standard deviation of the ratio of measured CAA capacity to the calculated one based on Park and Gamble (2000) were 1.37 and 0.38, respectively. Thus, Park and Gamble (2000)'s model may underestimate the CAA significantly. Similar conclusions were found by Lu et al. (2018). To reveal the reasons for this underestimation, the measured peak displacements (corresponding CAA capacity) were substituted into the model. As shown in Fig. 25b, the mean value and standard deviation of the ratio of the measured CAA to the calculated one were 1.10 and 0.23, respectively. Therefore, the underestimation of Park's model was mainly due to improperly assumption of the peak displacement as a constant value ($\delta=0.5h$). To improve the accuracy of Park and Gamble (2000)'s model, Lu et al. (2018) conducted comprehensive parametric studies based on validated finite element model (FEM). A regression model of $\delta=0.0005L^2/h$ was proposed by Lu et al. (2018). The calculated peak

365 displacements of the specimens are compared with the measured ones in Table 4. As shown in the
366 table, in general, the measured displacements are larger than the calculated ones, especially for
367 specimens with span-to-depth ratio less than 7, which could be explained as the regression model was
368 mainly calculated based on specimens with larger span-to-depth ratio. As shown in Fig. 25c, relied on
369 Lu et al. (2018)'s model, the mean value and standard deviation of the ratio of the measured CAA to
370 the analytical one was 1.04 and 0.23, respectively. If only look at the specimens with span-to-depth
371 ratio less than 7, the mean value was 1.16. Therefore, the regressed equation is more favorable for
372 specimens with relatively larger span-to-depth ratio (greater than 7). Moreover, if we only look at
373 HSC-series specimens in this study, the calculated CAA capacity of HSC-8, HSC-11, and HSC-13 was
374 112 %, 114 %, and 114 % of the measured one, respectively. Thus, Lu et al. (2018)'s model may
375 considerably overestimate the CAA capacity for the frames with high strength concrete as the
376 regression model ($\delta=0.0005L^2/h$) did not include the parameter of concrete strength.

377 **Assessment of the accuracy of existing TCA models**

378 As the last line of defense in resisting progressive collapse, TCA is undoubtedly the most
379 important mechanism to provide alternate load path. To effectively predict TCA capacity, Yi et al.
380 (2008), Su et al. (2009), and Yu and Tan (2013b) proposed simplified TCA models. In their models,
381 progressive collapse was assumed to be resisted by the tensile force in beam rebar. However, the
382 contribution of beam rebar for TCA capacity is different in different models. In Yi et al. (2008)'s
383 model, both the top and bottom rebar of beam are deemed to provide resistance. However, in Su et al.
384 (2009)'s model, only the bottom rebars are considered to provide resistance. Conversely, Yu and Tan
385 (2013b) assumed that the TCA capacity is purely provided by the top rebars. In this evaluation study,
386 the deformation capacity of each specimen is assumed to be 10% of the total span of the double-bay
387 beam, in accordance to DoD (2009). The TCA model of Yi et al. (2008), Su et al. (2009) and Yu and
388 Tan (2013b) can be expressed as Eqs. 10 -12, respectively.

$$389 \quad P_{TCA} = 2\psi(A_{st}f_y + A_{sb}f_y')\sin\alpha \quad (10)$$

390
$$P_{TCA} = 2A_{sb}f_y' \sin \varphi \quad (11)$$

391
$$P_{TCA} = 2A_{st}f_y \sin \alpha \quad (12)$$

392 where A_{st} and A_{sb} are the area of top and bottom rebars, respectively; f_y and f_y' are the yield
393 strength of top and bottom rebars, respectively; ψ is a strain adjustment coefficient, and $\psi=0.85$; α is
394 the chord rotation of beam; φ is the angle between the connection of top rebar at the side column stub
395 and bottom rebar at the middle column stub and the horizontal line.

396 A database consists of 30 specimens including the tests from literatures (Su et al. 2009, Yu and
397 Tan 2013b, Yu and Tan 2014, Qian et al. 2015, Alogla et al. 2016, Ren et al. 2016) and tested
398 specimens in this study was utilized to validate the reliability of the TCA models mentioned above. Fig.
399 26 shows the comparison of the measured TCA capacity with the calculated one. As shown in the
400 figure, the mean ratio of the measured TCA capacity to the calculated one based on the models of Yi et
401 al. (2008), Su et al. (2009), and Yu and Tan (2013b) was 1.06, 1.43 and 1.60, respectively. The
402 standard deviation was 0.28, 0.42 and 0.53, respectively. Thus, among them, the model of Yi et al.
403 (2008) gives the best prediction. The model of Su et al. (2009) neglected the contribution from top
404 rebars resulted in conservative prediction. However, as the model of Yu et al. (2013b) assuming the
405 bottom rebar was completely fractured, which is not in reality, the model may also underestimate the
406 resistance of TCA significantly.

407 For HSC-series specimens, the mean value of the ratio of measured TCA capacity to calculate
408 one from the models of Yi et al. (2008), Su et al. (2009), and Yu and Tan (2013b) was 0.94, 1.48 and
409 1.33, respectively. Therefore, different to the specimens using NSC, Yi et al. (2008)'s model
410 overestimates the TCA capacity of the specimens using HSC slightly. However, as the test data
411 collected from HSC specimens are very few and it is necessary to carry out further tests on HSC RC
412 frames to further support the conclusions.

413 CONCLUSIONS

414 Based on the results of the experimental and analytical investigation presented in this paper, the
415 following conclusions are drawn:

416 1. Test results indicated that for normal strength concrete frames, the CAA capacity and TCA
417 capacity increase by 79.0 % and 8.6 %, respectively, when the span-to-depth ratio decreased
418 from 13 to 8. For the frames with high strength concrete, the CAA capacity and TCA capacity,
419 increase by 89.5 % and 13.9 % respectively, when the span-to-depth ratio decreased from 13 to
420 8. Therefore, the span-depth-ratio has significant effect on CAA capacity but not for TCA
421 capacity.

422 2. Based on the test results, high strength concrete could increase the CAA capacity of the frame
423 with span-to-depth ratio of 8, 11, and 13 by 18.2 %, 15.4 %, and 11.6 %, respectively. Thus,
424 high strength concrete is beneficial to enhance CAA capacity, especially for the frames with
425 low span-to-depth ratio. However, the TCA capacity of specimen HSC-8, HSC-11, and HSC-
426 13 only achieved 93.2 %, 87.2 %, and 88.9 % of that of NSC-8, NSC-11, and NSC-13,
427 respectively. Thus, the specimens with high strength concrete may detriment the TCA capacity
428 due to high bond strength between reinforcements and concrete, which prone to premature the
429 fracture of reinforcements. However, it should be noted that non-seismically designed
430 specimens were tested. For seismically designed and detailed specimens, more tests should be
431 carried out on evaluation of the HSC effects.

432 3. Analytical evaluation indicated that Park's model will underestimate the CAA capacity
433 significantly due to improperly assumption of the peak displacement as $0.5h$. However, the
434 agreements could be improved for both NSC and HSC specimens significantly when the peak
435 displacement assumes to be $0.0005L^2/h$, in accordance to the study of Lu et al. (2018).
436 However, the model proposed by Lu et al. (2018) is more suit for RC frames with relatively
437 larger span-to-depth ratio (larger than 7). And Lu et al. (2018)'s model may overestimate the
438 CAA capacity of HSC-series specimens significantly due to the regression model did not
439 included the effects of concrete strength.

440 4. Although Yi et al. (2008)'s model produced the best prediction for TCA capacity, it slightly
441 underestimates the TCA capacity of NSC frames but overestimate that of HSC frames.
442 Although the models proposed by Yu and Tan (2013b) and Su et al. (2009) underestimate the
443 TCA capacity, the reason was different. For Su et al. (2009), the contribution of top
444 reinforcement is ignored, which disagrees with the test observation. However, for Yu and Tan
445 (2013b), the contribution of bottom reinforcements is neglected, which is over-conservative. In
446 reality, the bottom reinforcement may not fracture completely when the deformation reached
447 10 % of the total length of the double-span beams, which is proposed by the guideline of DoD
448 (2009).

449 **FUTURE RESEARCH**

450 Based on the test results and conclusions, the future research needed was highlighted. The effects of
451 HSC on seismically designed specimens should be evaluated in the future as the conclusions from non-
452 seismically designed specimens may not be suitable for seismically designed ones. Moreover, the
453 effects of different boundary conditions (different column missing scenarios) should be quantified.
454 Furthermore, the effects of HSC on dynamic response of RC moment frame subjected to suddenly
455 column removal should be investigated.

456 **DATA AVAILABILITY**

457 Some or all data, models, or code generated or used during the study are available from the
458 corresponding author by request (data related in the measured curves, photos, etc.).

459 **REFERENCES**

- 460 ASCE/SEI 7 (2010) "Minimum Design Loads for Buildings and Other Structures." Structural
461 Engineering Institute-American Society of Civil Engineers, Reston, VA, 424 pp.
- 462 ACI Committee 318 (2014), "Building Code Requirements for Structural Concrete (ACI 318-14) and
463 Commentary (318R-14)." American Concrete Institute, Farmington Hills, MI, 433 pp.

464 Alogla, K., Weekes, L., and Augusthus-Nelson, L. (2016) “A New Mitigation Scheme to Resist
465 Progressive Collapse of RC Structures.” *Construction and Building Materials*, 125: pp. 533–545.

466 BS8110 (1997), “Structural Use of Concrete Part 1: Code of Practice for Design and Construction.”
467 British Standard Institute, United Kingdom.

468 British Standards Institute (2006), “Eurocode 1: Actions on Structures. Part 1-7: General Actions-
469 Accidental Actions.” BS EN 1991-1-7: 2006, London.

470 Choi, H., and Kim, J. (2011). “Progressive Collapse-Resisting Capacity of RC Beam–Column Sub-
471 assemblage.” *Magazine of Concrete Research*, 63(4): pp. 297–310.

472 DoD (2009). “Design of Building to Resist Progressive Collapse.” Unified Facility Criteria, UFC 4-
473 023-03, U.S. Department of Defense, Washington, DC.

474 FarhangVesali, N., Valipour, H., Samali, B., and Foster, S. (2013). “Development of Arching Action
475 in Longitudinally-Restrained Reinforced Concrete Beams.” *Construction and Building Materials*,
476 47: pp. 7-19.

477 GSA (2009). “Progressive Collapse Analysis and Design Guidelines for New Federal Office Buildings
478 and Major Modernization Projects.” U.S. General Service Administration, Washington, DC.

479 Izzuddin, B. A., Vlassis, A. G., Elghazouli, A. Y., and Nethercot, D. A. (2008). “Progressive Collapse
480 of Multi-Storey Buildings due to Sudden Column Loss—Part I: Simplified Assessment
481 Framework.” *Engineering Structures*, 30(5): pp. 1308–1318.

482 Kim, J., and An, D. (2009). “Evaluation of Progressive Collapse Potential of Steel Moment Frames
483 Considering Catenary Action.” *The Structural Design of Tall and Special Buildings*, 18(4): pp.
484 455-465.

485 Kim, J., Choi, H., and Min, K.W. (2011). “Use of Rotational Friction Dampers to Enhance Seismic
486 and Progressive Collapse Resisting Capacity of Structures.” *The Structural Design of Tall and
487 Special Buildings*, 20(4): pp.515-537.

488 Kim, J., and Choi, H. (2016). “Monotonic Loading Tests of RC Beam-Column Subassemblage
489 Strengthened to Prevent Progressive Collapse.” *International Journal of Concrete Structures and*
490 *Materials*, 9(4): pp. 401-413.

491 Lew, H. S., Bao, Y. H., Pujol, S., and Sozen, M. A. (2014). “Experimental Study of Reinforced
492 Concrete Assemblies under Column Removal Scenario.” *ACI Structural Journal*, 111(4): pp. 881-
493 892.

494 Lu, X. Z., Lin, K. Q., Li, Y., Guan, H., Ren, P. Q., and Zhou, Y. L. (2017). “Experimental
495 Investigation of RC Beam-Slab Substructures against Progressive Collapse Subject to an Edge-
496 Column Removal Scenario.” *Engineering Structures*, 149: pp. 91-103.

497 Lu, X. Z., and Li, K. Q., Li, C. F., and Li, Y. (2018). “New Analytical Calculation Models for
498 Compressive Arch Action in Reinforced Concrete Structures.” *Engineering Structures*, 168: pp.
499 721-735.

500 Orton, S., Jirsa, J. O., and Bayrak, O. (2009). “Carbon Fiber-Reinforced Polymer for Continuing in
501 Existing Reinforced Concrete Buildings Vulnerable to Collapse.” *ACI Structural Journal*, 106(5):
502 pp. 608-616.

503 Park, R., and Gamble, W. L. (2000). “Reinforced Concrete Slabs.” Wiley, New York.

504 Peng, Z. H., Orton, S. L., Liu, J. R., and Tian, Y. (2017). “Experimental Study of Dynamic Progressive
505 Collapse in Flat-Plate Buildings subjected to Exterior Column Removal.” *Journal of Structural*
506 *Engineering*, 143(9): 04017125.

507 Qian, K. and Li, B. (2012a). “Slab Effects on the Response of Reinforced Concrete Substructures after
508 Loss of Corner Column.” *ACI Structural Journal*, 109(6): pp. 845-855.

509 Qian, K., and Li, B. (2012b). “Dynamic Performance of RC Beam-Column Substructures under the
510 Scenario of the Loss of a Corner Column—Experimental Results.” *Engineering Structures*, 42: pp.
511 154-167.

512 Qian, K., and Li, B. (2012c). “Experimental and Analytical Assessment on RC Interior Beam-Column
513 Subassemblages for Progressive Collapse.” *Journal of Performance of Constructed Facilities*,
514 ASCE, 26(5): pp. 576-589.

515 Qian, K., and Li, B. (2015a). “Quantification of Slab Influence on the Dynamic Performance of RC
516 Frames against Progressive Collapse.” *Journal of Performance of Constructed Facilities*, ASCE,
517 29(1): 04014029.

518 Qian, K., and Li, B. (2015b). “Research Advances in Design of Structures to Resist Progressive
519 Collapse.” *Journal of Performance of Constructed Facilities*, ASCE, 29(5): B4014007.

520 Qian, K., Li, B., and Ma, J.-X. (2015). “Load-Carrying Mechanism to Resist Progressive Collapse of
521 RC Buildings.” *Journal of Structural Engineering*, 141(2): 04014107.

522 Qian, K., Li, B., and Zhang, Z. (2016). “Influence of Multicolumn Removal on the Behavior of RC
523 Floors.” *Journal of Structural Engineering*, 142(5): 04016006.

524 Qian, K., and Li, B. (2017). “Effects of Masonry Infill Wall on the Performance of RC Frames to
525 Resist Progressive Collapse.” *Journal of Structural Engineering*, 143(9): 04017118.

526 Qian, K., Liu, Y., Yang, T., and Li, B. (2018). “Progressive Collapse Resistance of Posttensioned
527 Concrete Beam-Column Subassemblages with Unbonded Posttensioning Strands.” *Journal of*
528 *Structural Engineering*, 144(1): 04017182.

529 Qian, K., Weng, Y. H., and Li, B. (2019). “Improving Behavior of Reinforced Concrete Frames to
530 Resist Progressive Collapse through Steel Bracings.” *Journal of Structural Engineering*, 145(2):
531 04018248.

532 Ren, P. Q., Li, Y., Lu, X. Z., Guan, H., and Zhou, Y. L. (2016). “Experimental Investigation of
533 Progressive Collapse Resistance of One-Way Reinforced Concrete Beam-Slab Substructures under
534 a Middle-Column-Removal Scenario.” *Engineering Structures*, 118: pp. 28–40.

535 Su, Y. P., Tian, Y., and Song, X. S. (2009). “Progressive Collapse Resistance of Axially-Restrained
536 Frame Beams.” *ACI Structural Journal*, 106(5): pp. 600-607.

- 537 Sasani, M., Kazemi, A., Sagioglu, S., and Forest, S. (2011a). "Progressive Collapse Resistance of an
538 Actual 11-Story Structure Subjected to Severe Initial Damage." *Journal of Structural Engineering*,
539 137(9): pp. 893-902.
- 540 Sasani, M., Werner, A., and Kazemi, A. (2011b) "Bar Fracture Modeling in Progressive Collapse
541 Analysis of Reinforced Concrete Structures." *Engineering Structures*, 33(2): pp. 401–409.
- 542 Tsai, M. H. (2010). "An Analytical Methodology for the Dynamic Amplification Factor in Progressive
543 Collapse Evaluation of Building Structures." *Mechanics Research Communications*, 37(1): pp. 61-
544 66.
- 545 Valipour, H., Vessali, N., Foster, S.J., and Samali, B. (2015a). "Influence of Concrete Compressive
546 Strength on the Arching Behaviour of Reinforced Concrete Beam Assemblages." *Advances in*
547 *Structural Engineering*, 18(8): pp. 1199-1214.
- 548 Valipour, H., Vessali, N., and Foster, S.J. (2015b). "Fibre-reinforced Concrete Beam Assemblage
549 Subject to Column Loss." *Magazine of Concrete Research*, 68 (6): pp. 305-317.
- 550 Valipour, H., Rajabi, A., Foster, S.J., and Bradford, M. A. (2015c). "Arching Behavior of precast
551 Concrete Slabs in a Deconstructible Composite Bridge Deck." *Construction and Building*
552 *Materials*, 87: pp. 67-77.
- 553 Xiao, Y., Kunnath, S., Li, F. W., Zhao, Y. B., Lew, H. S., and Bao, Y. (2015). "Collapse Test of
554 Three-Story Half-Scale Reinforced Concrete Frame Building." *ACI Structural Journal*, 112(4): pp.
555 429-438.
- 556 Yi, W. J., He, Q. F., Xiao, Y., and Kunnath, S. K. (2008). "Experimental Study on Progressive
557 Collapse-Resistant Behavior of Reinforced Concrete Frame Structures." *ACI Structural Journal*,
558 105(4): pp. 433-439.
- 559 Yap, L. S., and Li, B. (2011). "Experimental Investigation of Reinforced Concrete Exterior Beam-
560 Column Subassemblages for Progressive Collapse." *ACI Structural Journal*, 108(5): pp. 542-552.

561 Yu, J., and Tan, K. H. (2013a). “Experimental and Numerical Investigation on Progressive Collapse
562 Resistance of Reinforced Concrete Beam Column Sub-assemblages.” *Engineering Structures*, 55:
563 pp. 90-106.

564 Yu, J., Tan, K. H. (2013b). “Structural Behavior of RC Beam-Column Sub-assemblages under a
565 Middle Column Removal Scenario.” *Journal of Structural Engineering*, 139(2): pp. 233–250.

566 Yu, J., and Tan, K. H. (2014). “Special Detailing Techniques to Improve Structural Resistance against
567 Progressive Collapse.” *Journal of Structural Engineering*, 140(3): 04013077.

568 Yu, J., Rinder, T., Stolz, A., Tan, K. H., and Riedel, W. (2014). “Dynamic Progressive Collapse of an
569 RC Assemblage Induced by Contact Detonation.” *Journal of Structural Engineering*, 140(6):
570 04014014.

571

572 **FIGURE CAPTIONS**

573

574 **Fig. 1.** Dimension and reinforcement details of Specimen NSC-11: (a) elevation view; (b) cross

575 sections

576 **Fig. 2.** Test setup and instrumentation layout of the tests: (a) photo; (b) schematic view

577 **Fig. 3.** Vertical load-displacement history: (a) NSC-series; (b) HSC-series

578 **Fig. 4.** Crack pattern: (a) NSC-11; (b) HSC-11

579 **Fig. 5.** Failure mode of Specimen NSC-11

580 **Fig. 6.** Failure mode of Specimen NSC-13

581 **Fig. 7.** Failure mode of Specimen NSC-8

582 **Fig. 8.** Failure mode of Specimen HSC-11

583 **Fig. 9.** Failure mode of Specimen HSC-13

584 **Fig. 10.** Failure mode of Specimen HSC-8

585 **Fig. 11.** Horizontal reaction force-displacement curves: (a) NSC series; (b) HSC series

586 **Fig. 12.** Deformation shape of the beams of Specimen NSC-11 at various stages

587 **Fig. 13.** Strain gauge results of NSC-11: (a) top beam rebar; (b) bottom beam rebar

588 **Fig. 14.** Strain gauge results of HSC-11: (a) top beam rebar; (b) bottom beam rebar

589 **Fig. 15.** Strain gauge results of HSC-8: (a) top beam rebar; (b) bottom beam rebar

590 **Fig. 16.** Dynamic performance of the specimens

591 **Fig. 17.** Relationship of internal forces and the load resistance

592 **Fig. 18.** Collapse Resistance contributions from axial and shear force: (a) NSC-11; (b) HSC-11; (c)

593 NSC-8; (d) HSC-8

594 **Fig. 19.** Variations of bending moments v.s. deflections at different cross-section: (a) NSC-11; (b)

595 HSC-11; (c) NSC-8; (d) HSC-8

596 **Fig. 20.** M-N relationship at the beam end of NSC-11: (a) nearby the middle column; (b) nearby the

597 side column

598 **Fig. 21.** M-N relationship at the beam end of NSC-8: (a) nearby the middle column; (b) nearby the side

599 column

600 **Fig. 22.** M-N relationship at the beam end of HSC-11: (a) nearby the middle column; (b) nearby the

601 side column

602 **Fig. 23.** M-N relationship at the beam end of HSC-8: (a) nearby the middle column; (b) nearby the side

603 column

604 **Fig. 24.** Internal Force diagram for derivation of the analytical model of CAA

605 **Fig. 25.** Comparison of the measured CAA capacity with calculated one: (a) $\delta=0.5h$; (b) measured δ ;

606 (c) $\delta=0.0005L^2/h$

607 **Fig. 26.** Comparison of the measured TCA capacity with calculated one: (a) Yi et al. (2008); (b) Su et

608 al. (2009); (c) Yu and Tan (2013b)

609

610

611

612

613

614

615

616

617

618
619
620
621
622
623
624
625
626
627
628
629
630
631
632
633
634
635
636
637
638
639
640
641
642

643

644

Table 1-Specimen properties

Test ID	Beam clear span (mm)	Beam longitudinal reinforcement				Concrete
		A-A section		B-B section		
		Top	Bottom	Top	Bottom	
NSC-8	2000	3T12	2T12	2T12	2T12	Normal strength
NSC-11	2750	3T12	2T12	2T12	2T12	Normal strength
NSC-13	3250	3T12	2T12	2T12	2T12	Normal strength
HSC-8	2000	3T12	2T12	2T12	2T12	High strength
HSC-11	2750	3T12	2T12	2T12	2T12	High strength
HSC-13	3250	3T12	2T12	2T12	2T12	High strength

645

646

Table 2-Material properties of reinforcements

Items		Nominal diameter (mm)	Yield strength (MPa)	Ultimate strength (MPa)	Elongation (%)
Transverse reinforcement	R6	6	348	486	25.4
Longitudinal Reinforcements	T12	12	438	577	16.6
	T16	16	442	605	16.0

647

648

Note: R6 represents plain bar of with diameter of 6 mm; T12 and T16 represent deformed rebar with diameter of 12 mm and 16 mm, respectively.

649

Table 3-Test results

Test ID	Critical displacements (mm)			Critical loads (kN)			MHCF (kN)	MHTF (kN)
	YL	CAA	TCA	YL	CAA	TCA		
NSC-8	25	79	581	53	77	88	-202	147
NSC-11	36	90	712	37	52	94	-178	154
NSC-13	45	108	731	33	43	81	-153	148
HSC-8	16	80	547	56	91	82	-321	145
HSC-11	28	74	663	42	60	80	-259	142
HSC-13	35	104	701	36	48	72	-233	150

Note: YL means yielding load capacity; CAA represents CAA capacity; TCA represents TCA capacity; MHCF means maximum horizontal compressive force; and MHTF means maximum horizontal tensile force.

654

655

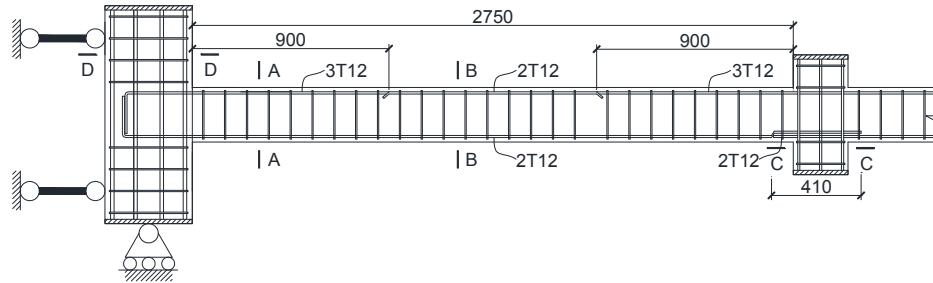
656

Table 4-Summary of key parameters and analytical results of CAA

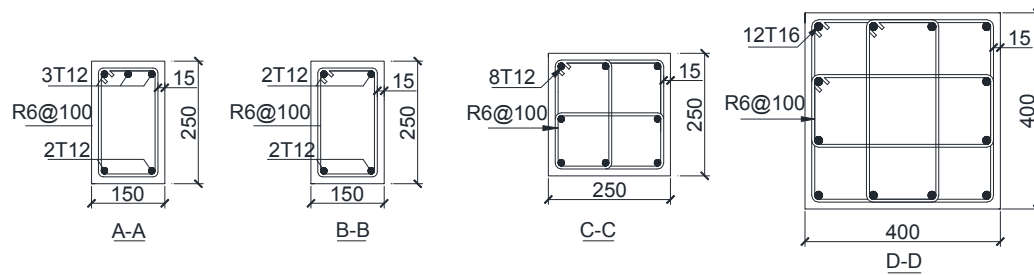
Test	ID	Lateral stiffness (kN/m)	Total length (mm)	Span to depth ratio	Beam section	Beam rebar		Material properties		Test results		Calculated results			
					h×b (mm×mm)	Top (mm)	Bottom (mm)	f_c' (MPa)	f_y (MPa)	Δ (mm)	P (kN)	Δ_L (mm)	$P_{\delta M}^*$ (kN)	$P_{\delta L}^\#$ (kN)	$P_{\delta p}^\$$ (kN)
This Test	NSC-8	1×10^5	4250	8.0	250×150	3Φ12	2Φ12	31.7	438	78.6	69.2	36.1	69.3	79.2	57.1
	NSC-11	1×10^5	5750	11.0	250×150	3Φ12	2Φ12	31.1	438	89.8	46.3	66.1	48.4	52.5	42.2
	NSC-13	1×10^5	6750	13.0	250×150	3Φ12	2Φ12	30.5	438	108.1	36.3	91.1	38.1	40.5	35.7
	HSC-8	1×10^5	4250	8.0	250×150	3Φ12	2Φ12	60.5	438	80.4	87.6	36.1	84.5	98.2	70.8
	HSC-11	1×10^5	5750	11.0	250×150	3Φ12	2Φ12	61.2	438	90.3	56.8	66.1	59.2	65.0	52.3
	HSC-13	1×10^5	6750	13.0	250×150	3Φ12	2Φ12	59.3	438	103.8	43.6	91.1	46.6	49.6	43.7
Su et al. (2009)	A1	1×10^6	2700	4.1	300×150	2Φ12	2Φ12	25.8	350	48.9	168.0	12.2	130.3	145.3	82.3
	A2	1×10^6	2700	4.1	300×150	3Φ12	3Φ12	28.2	350	56.4	221.0	12.2	159.5	180.3	109.9
	A3	1×10^6	2700	4.1	300×150	3Φ14	3Φ14	31.2	340	76.4	246.0	12.2	180.3	215.1	138.3
	A4	1×10^6	2700	4.1	300×150	2Φ12	1Φ14	23.0	350	65.0	147.0	12.2	104.6	126.7	68.0
	A5	1×10^6	2700	4.1	300×150	3Φ12	2Φ12	26.5	350	70.7	198.0	12.2	132.7	160.3	93.9
	A6	1×10^6	2700	4.1	300×150	3Φ14	2Φ14	28.6	340	69.2	226.0	12.2	159.5	188.0	116.8
	B1	1×10^6	4200	6.6	300×150	3Φ14	3Φ14	18.6	340	100.0	125.0	29.4	91.3	107.6	80.8
	B2	1×10^6	5700	9.1	300×150	3Φ14	3Φ14	19.3	340	102.0	82.9	54.2	64.6	75.7	60.0
	B3	1×10^6	5700	9.1	300×150	3Φ14	2Φ14	21.1	340	85.5	74.7	54.2	63.0	68.6	51.8
	C1	1×10^6	2700	6.1	200×100	2Φ12	2Φ14	15.9	350	33.7	60.9	18.2	44.5	46.7	35.7
	C2	1×10^6	2700	6.1	200×100	2Φ12	2Φ12	16.8	350	33.5	64.9	18.2	45.3	47.5	36.0
	C3	1×10^6	2700	6.1	200×100	2Φ12	2Φ12	16.3	350	28.7	68.6	18.2	45.6	47.1	35.8
Choi et al. (2011)	5S	N/A	3315	6.7	225×150	5Φ10	2Φ10	17.0	493	103.0	39.9	24.4	57.6	71.7	57.2
	5G	N/A	3325	8.2	185×150	2Φ10	2Φ10	17.0	493	84.5	22.8	29.9	30.6	48.2	30.3
	8S	N/A	3315	7.7	195×140	5Φ10	3Φ10	30.0	493	59.3	54.1	28.2	70.0	76.6	61.6
	8G	N/A	3325	9.4	160×125	2Φ10	2Φ10	30.0	493	59.0	23.7	34.5	29.4	33.4	26.3
Sasani et al. (2011)	P1	N/A	4170	10.4	190×190	5Φ9.5	2Φ9.5	41.0	516	41.0	71.8	45.8	44.9	60.7	44.1
Yu and Tan (2013b)	S1	1.06×10^5	5750	11.0	250×150	2Φ10 1Φ13	2Φ10	31.2	511	78.0	41.6	66.1	47.9	50.0	39.8
	S2	1.06×10^5	5750	11.0	250×150	3Φ10	2Φ10	31.2	511	73.0	38.4	66.1	45.7	46.9	36.7
	S3	4.29×10^5	5750	11.0	250×150	3Φ13	2Φ10	38.2	511	74.4	54.5	66.1	59.8	61.7	48.1
	S4	4.29×10^5	5750	11.0	250×150	3Φ13	2Φ13	38.2	494	81.0	63.2	66.1	64.9	68.3	54.8
	S5	4.29×10^5	5750	11.0	250×150	3Φ13	3Φ13	38.2	494	74.5	70.3	66.1	75.4	77.4	63.8
	S6	4.29×10^5	5750	11.0	250×150	3Φ16	2Φ13	38.2	494	114.4	70.3	66.1	66.8	78.0	64.4
	S7	4.29×10^5	4550	8.6	250×150	3Φ13	2Φ13	38.2	494	74.4	82.8	41.4	84.5	94.4	69.1

	S8	4.29×10^5	3350	6.2	250×150	3Φ13	2Φ13	38.2	494	45.9	121.3	22.4	128.3	136.6	93.4
Yu and Tan (2014)	F1-CD	4.29×10^5	5750	11.0	250×150	3Φ13	2Φ13	27.5	488	87.0	51.1	66.1	56.8	60.5	50.3
	F2-MR	4.29×10^5	5750	11.0	250×150	3Φ13	2Φ13	27.5	488	51.0	62.8	66.1	63.1	60.5	50.3
Farhang Vesali et al. (2013)	1	N/A	4400	11.7	180×180	2Φ10	2Φ10	30.5	620	49.0	40.5	53.8	36.9	36.0	29.4
	2	N/A	4400	11.7	180×180	2Φ10	2Φ10	27.0	620	44.0	35.7	53.8	35.7	34.4	28.5
	3	N/A	4400	11.7	180×180	2Φ10	2Φ10	30.0	620	50.0	41.4	53.8	36.5	35.8	29.3
	4	N/A	4400	11.7	180×180	3Φ10	3Φ10	26.0	620	54.0	40.1	53.8	38.6	38.7	32.9
	5	N/A	4400	11.7	180×180	3Φ10	3Φ10	29.5	620	54.0	41.6	53.8	40.3	40.3	33.9
	6	N/A	4400	11.7	180×180	3Φ10	3Φ10	30.0	620	52.0	39.4	53.8	40.9	34.1	34.0
Qian et al. (2015)	P1	N/A	4000	10.5	180×100	2Φ10	2Φ10	19.9	437	35.8	31.6	44.4	24.6	23.8	19.5
	P2	N/A	2800	9.3	140×80	2Φ10	2Φ10	20.8	437	32.9	35.5	28.0	21.0	21.4	17.7
Valipour et al. (2015a)	No. 1	N/A	4400	11.7	180×180	3Φ10	2Φ10	67.0	480	59.0	51.3	53.8	48.8	47.2	38.0
	No. 2	N/A	4400	11.7	180×180	2Φ10	2Φ10	67.0	480	54.8	42.5	53.8	46.4	43.3	34.1
	No. 3	N/A	4400	11.7	180×180	3Φ10	2Φ10	48.0	480	55.4	47.4	53.8	43.2	41.3	33.4
	No. 4	N/A	4400	11.7	180×180	2Φ10	2Φ10	48.0	480	56.3	38.5	53.8	39.1	37.4	29.5
Ren et al. (2016)	B2	N/A	4000	9.5	175×85	2Φ8 1Φ6	2Φ8	35.2	450	33.0	34	40.0	23.6	22.0	16.6
	B3	N/A	4000	10.9	200×85	2Φ8 1Φ6	2Φ8	35.2	450	33.3	41.0	45.7	30.7	29.7	20.6
Alogla et al. (2016)	SS1	N/A	5750	11.1	250×150	3Φ10	2Φ10	19.4	510	101.0	34.0	66.1	35.1	39.1	32.4
	SS2	N/A	5750	11.1	250×150	3Φ10	2Φ10	19.4	510	96.8	37.9	66.1	35.6	39.1	32.4
	SS3	N/A	5750	11.1	250×150	3Φ10	2Φ10	19.9	510	86.8	37.2	66.1	37.1	39.5	32.6
	SS4	N/A	5750	11.1	250×150	3Φ10	2Φ10	19.9	510	91.4	36.7	66.1	36.5	39.5	32.6

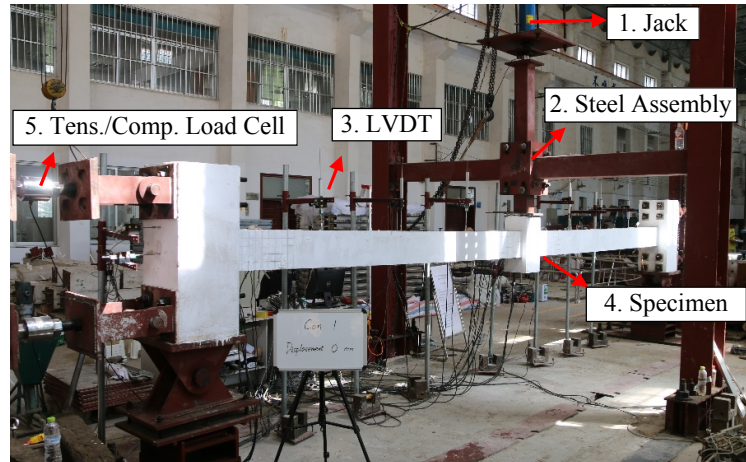
657 Note: Δ_L represents peak displacement proposed by Lu et al. (2018); $P_{\delta M}^*$, $P_{\delta L}^\#$, and $P_{\delta p}^s$ represent the calculated CAA capacity in accordance with the measured peak
658 displacement, peak displacement proposed by Lu et al. (2018), and peak displacement proposed by Park and Gamble (2000), respectively.



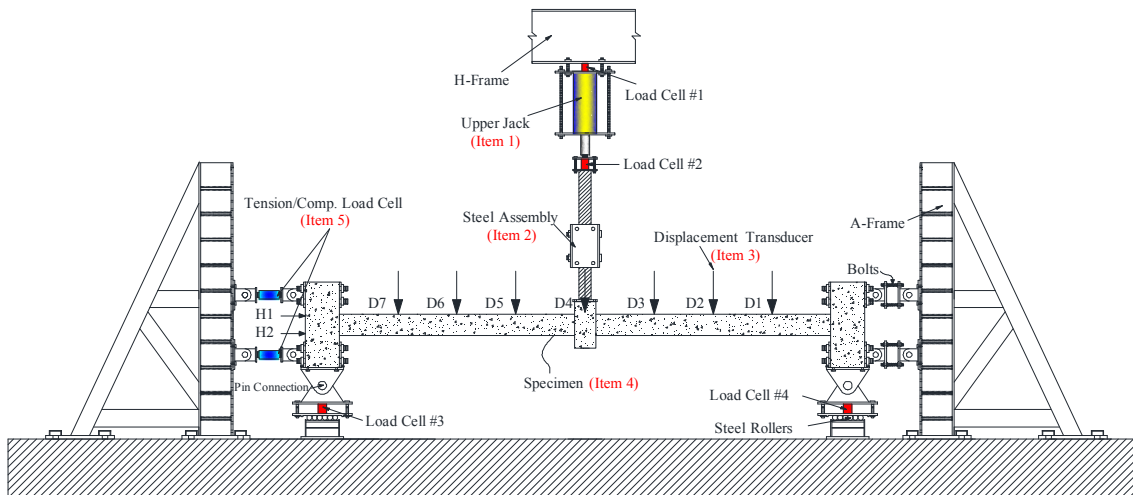
(a)



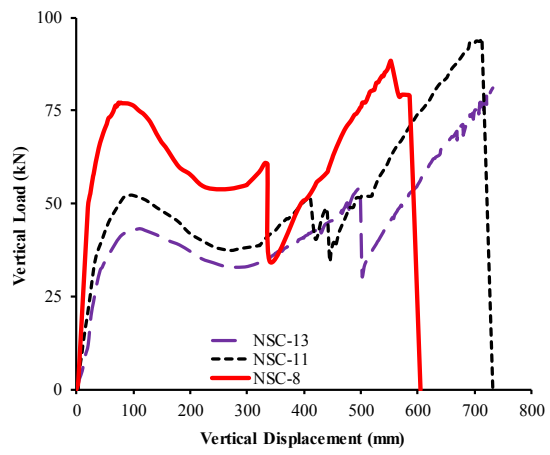
(b)



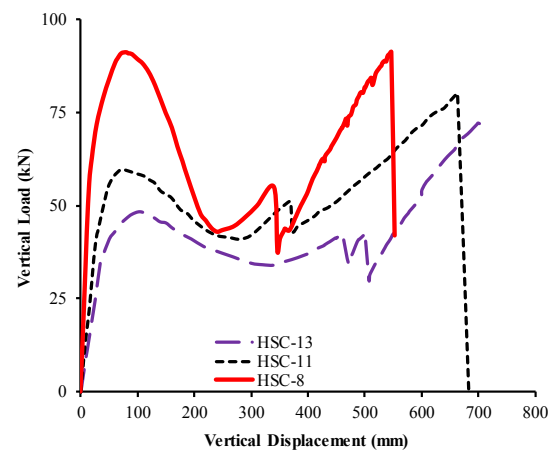
(a)



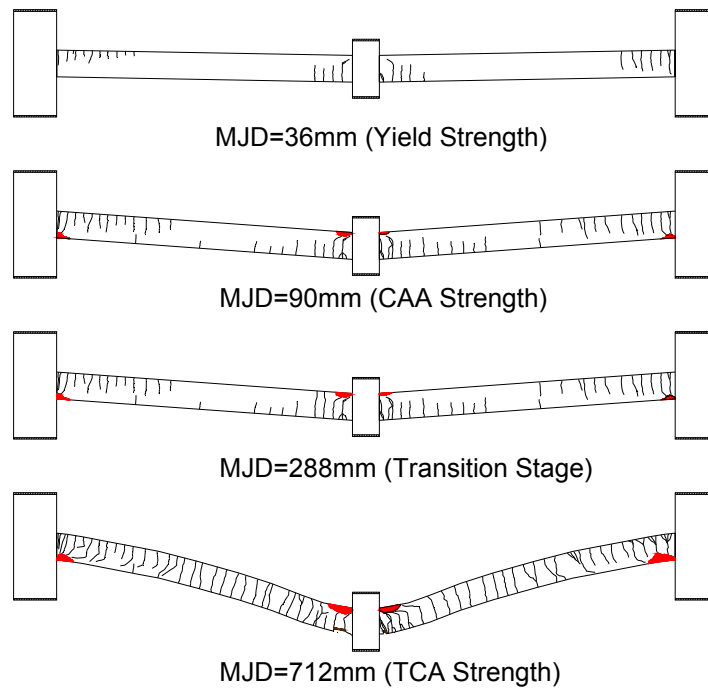
(b)



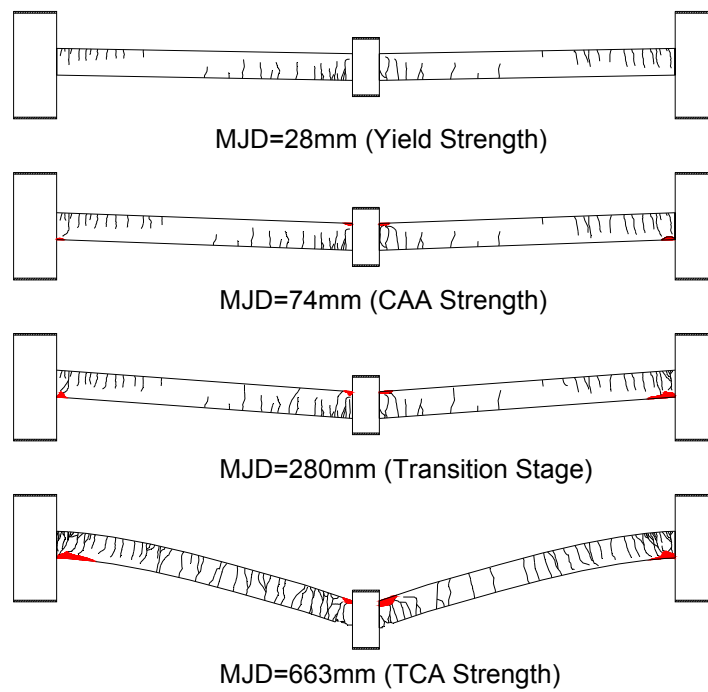
(a)



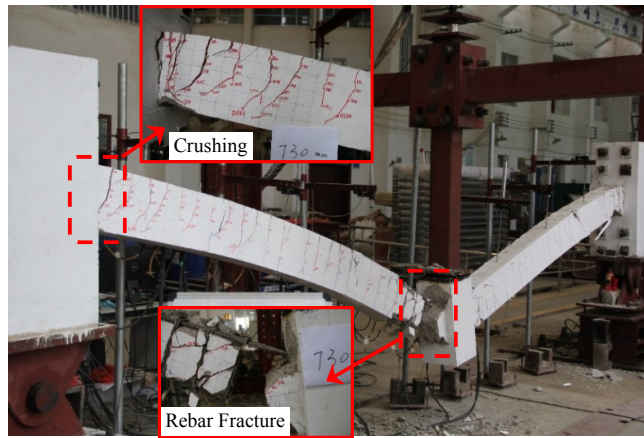
(b)

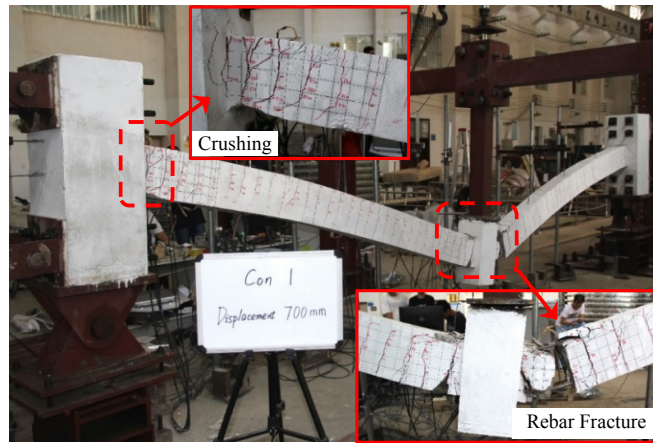


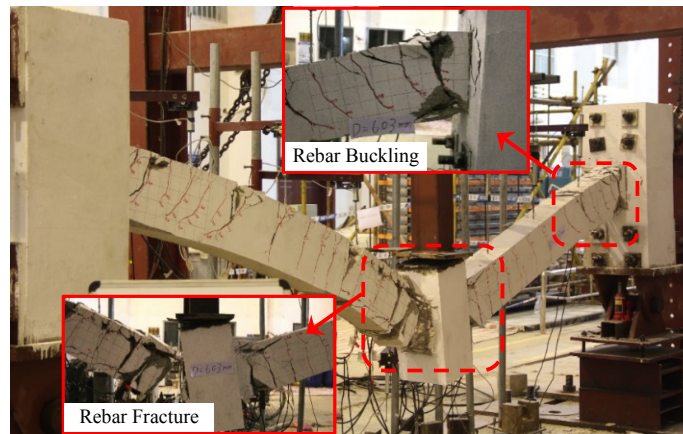
(a)

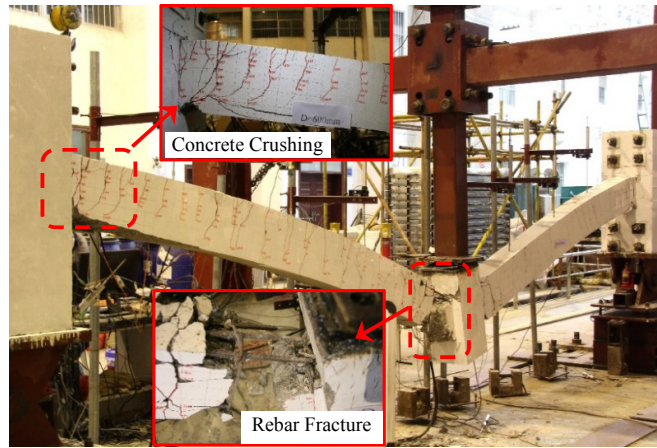


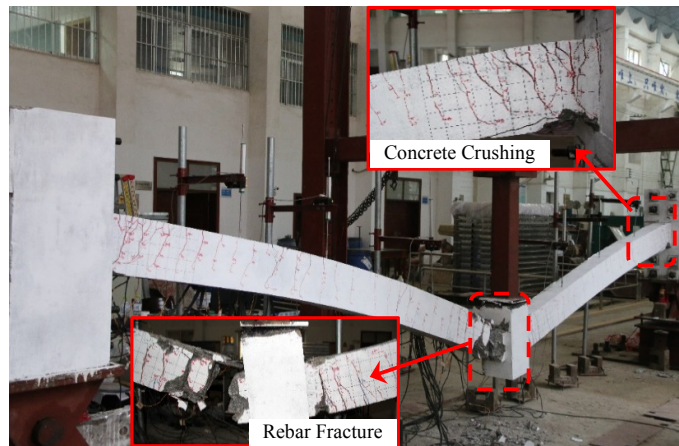
(b)

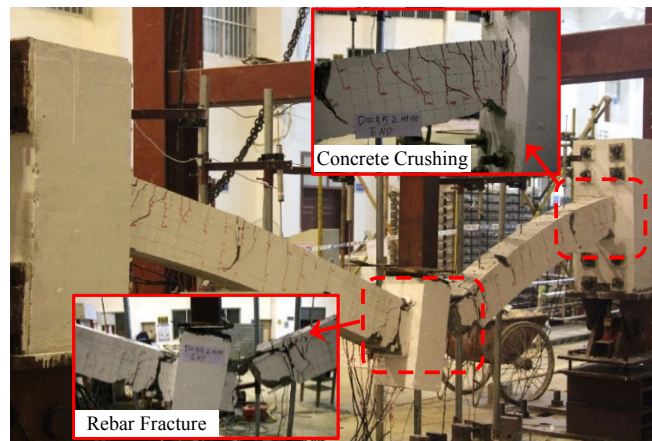


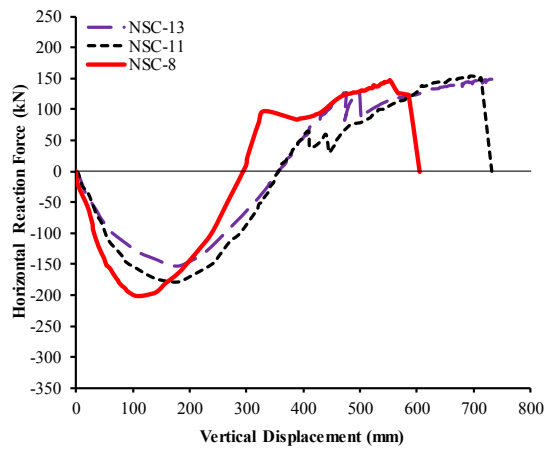




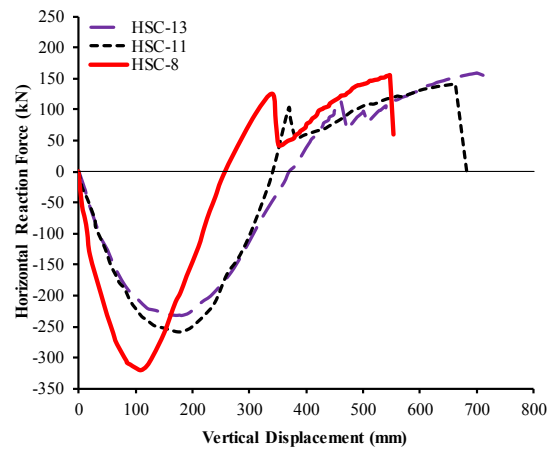




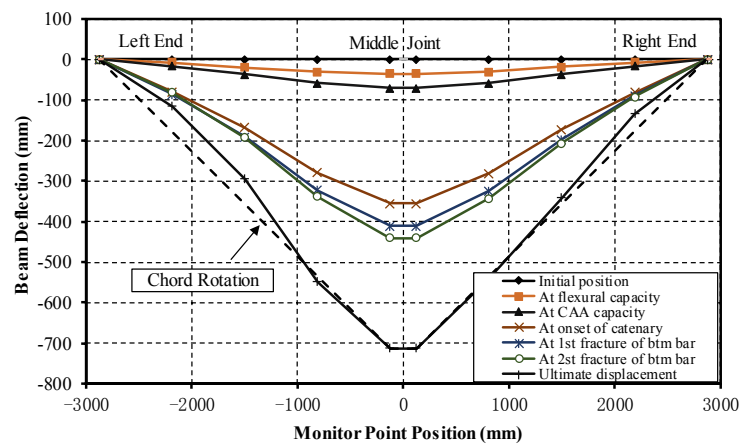


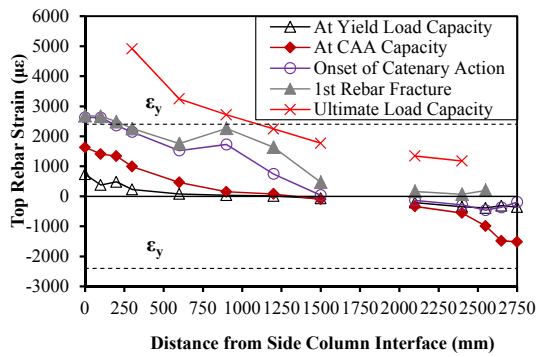


(a)

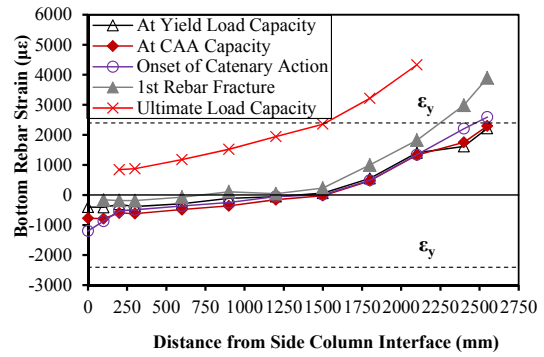


(b)

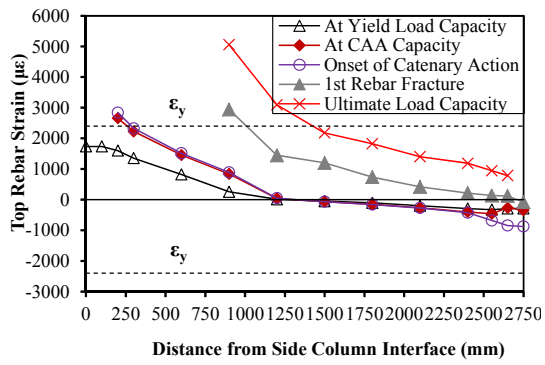




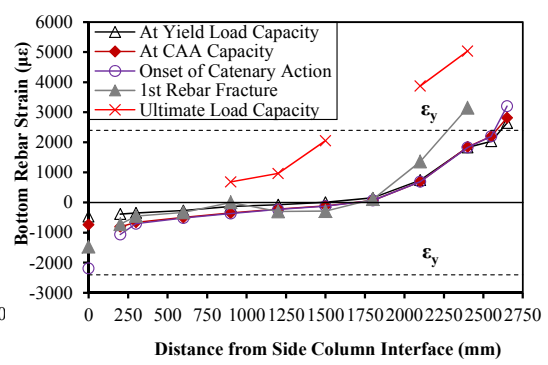
(a)



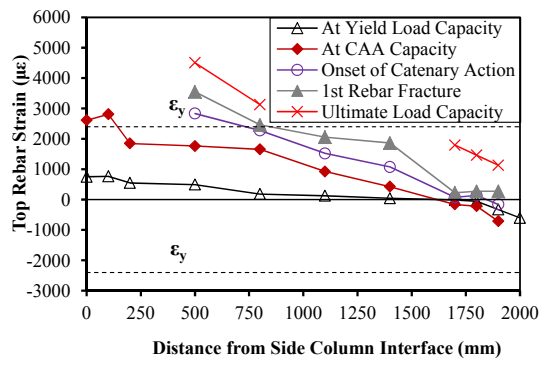
(b)



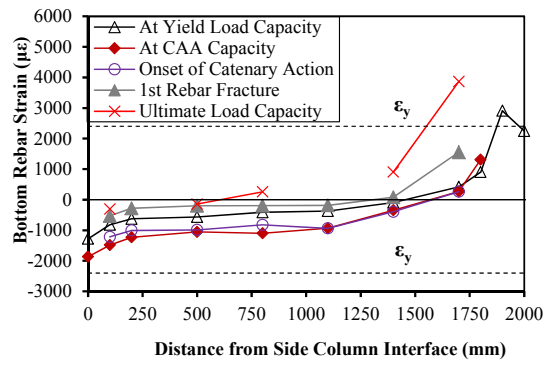
(a)



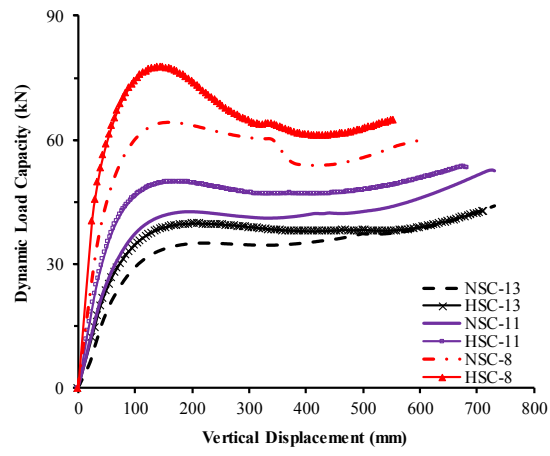
(b)

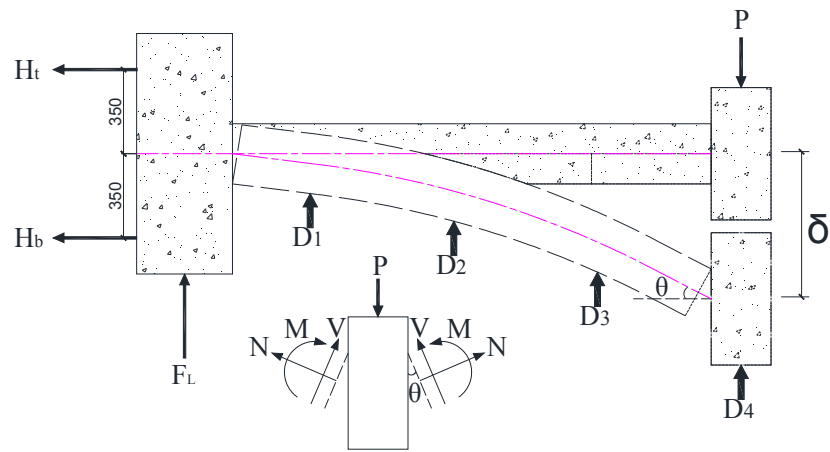


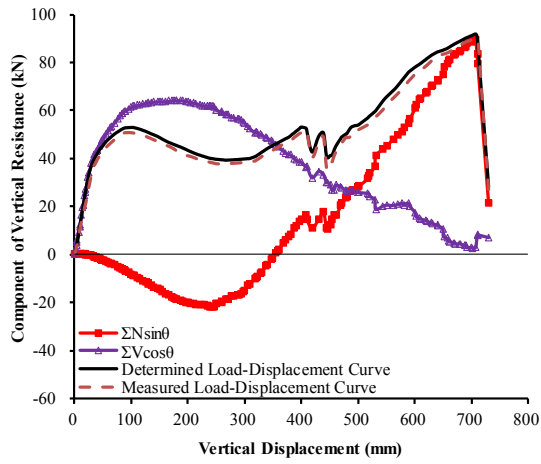
(a)



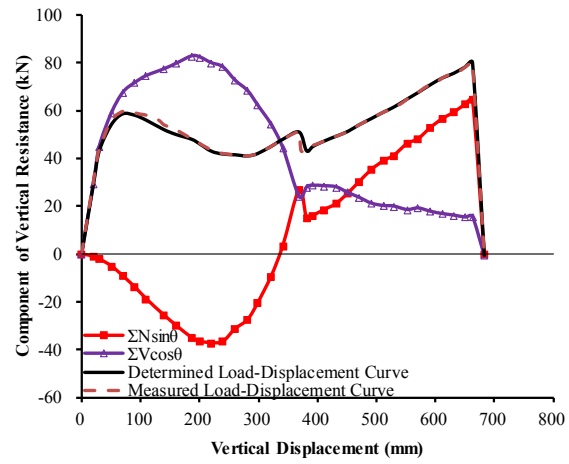
(b)



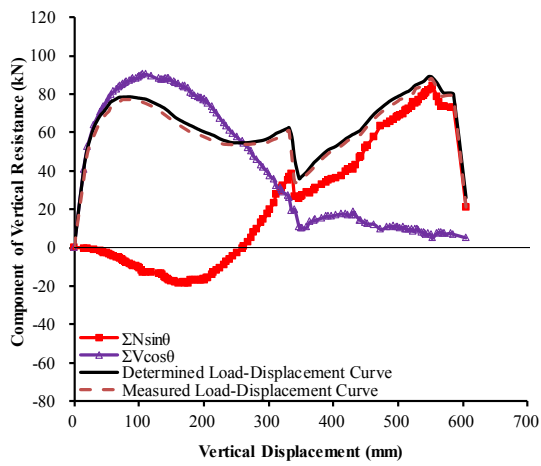




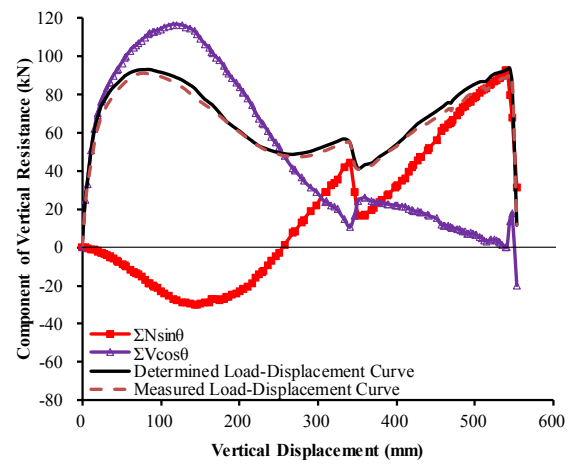
(a)



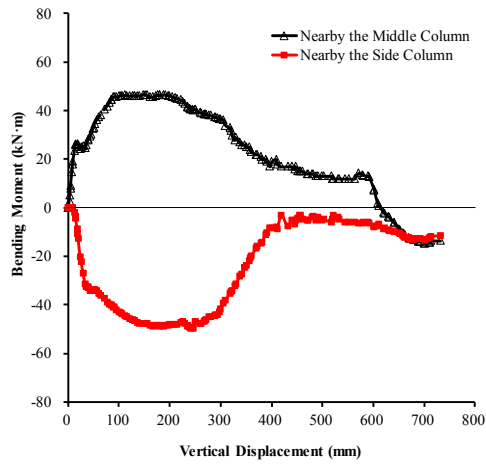
(b)



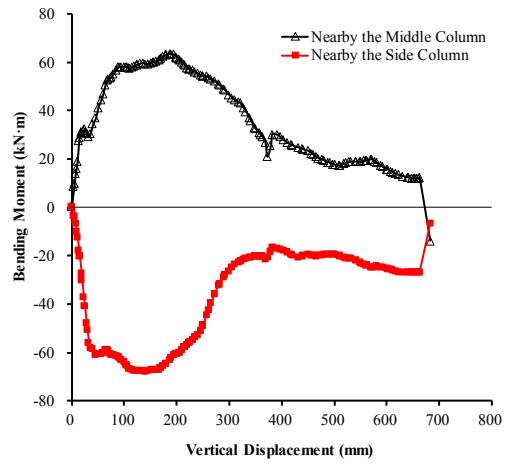
(c)



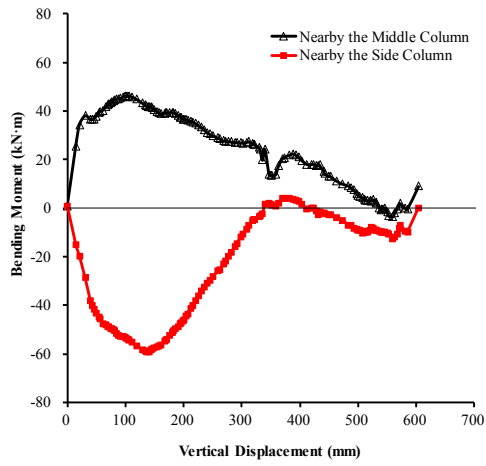
(d)



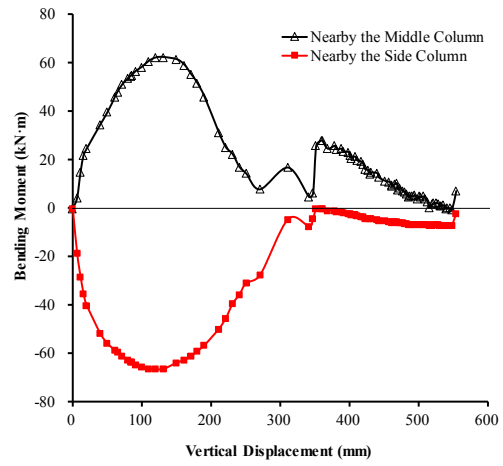
(a)



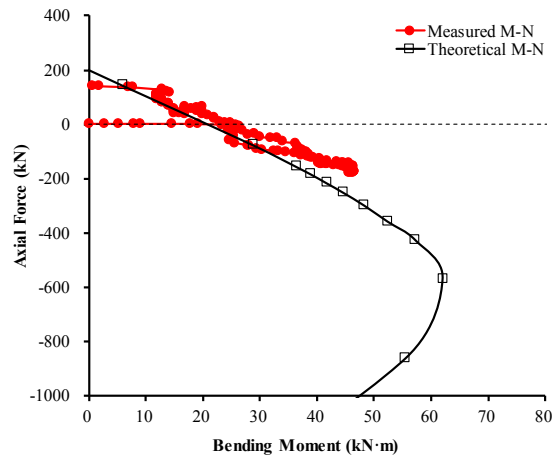
(b)



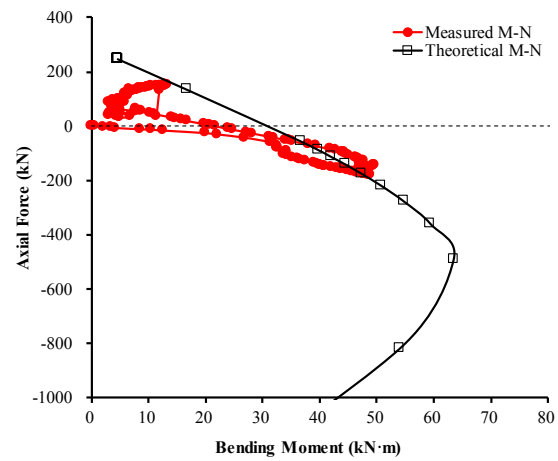
(c)



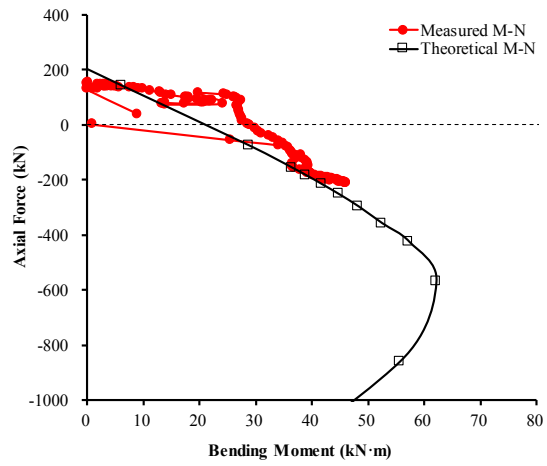
(d)



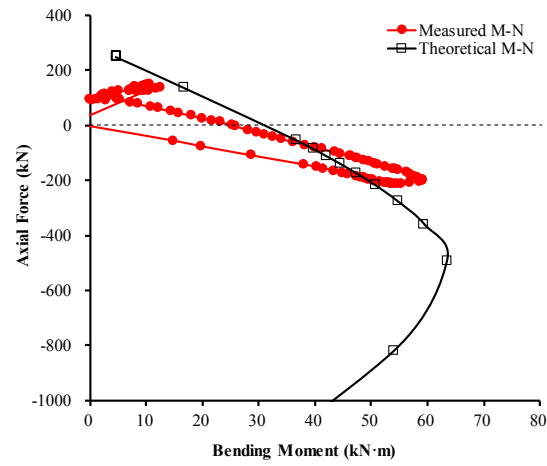
(a)



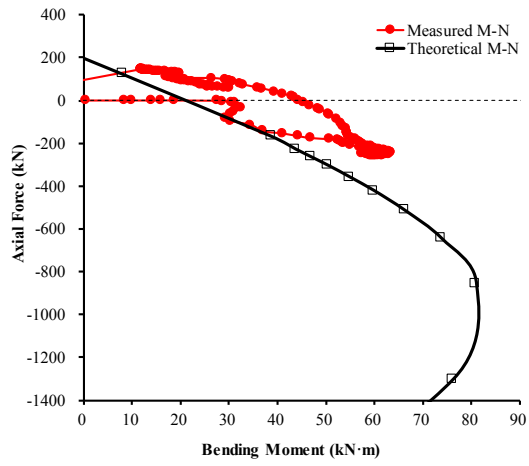
(b)



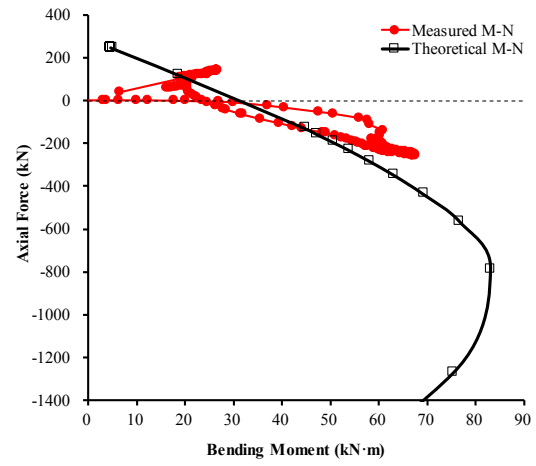
(a)



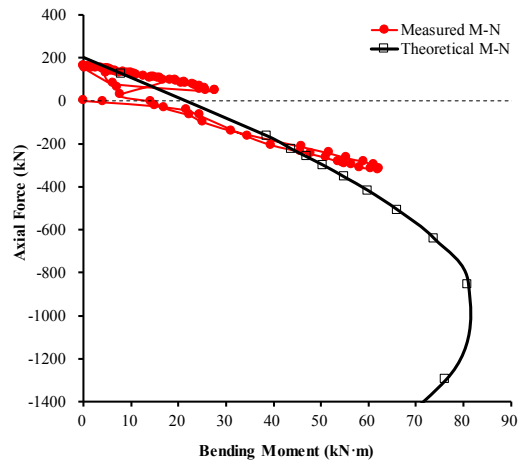
(b)



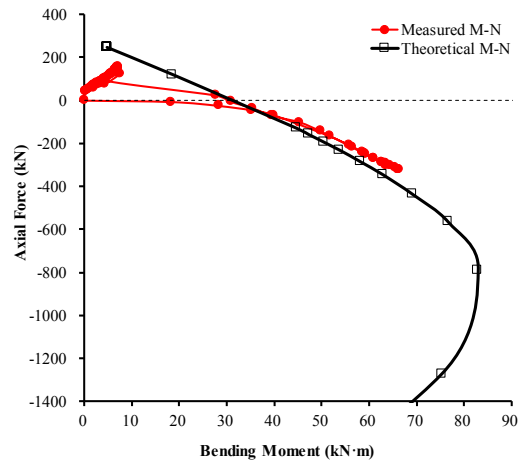
(a)



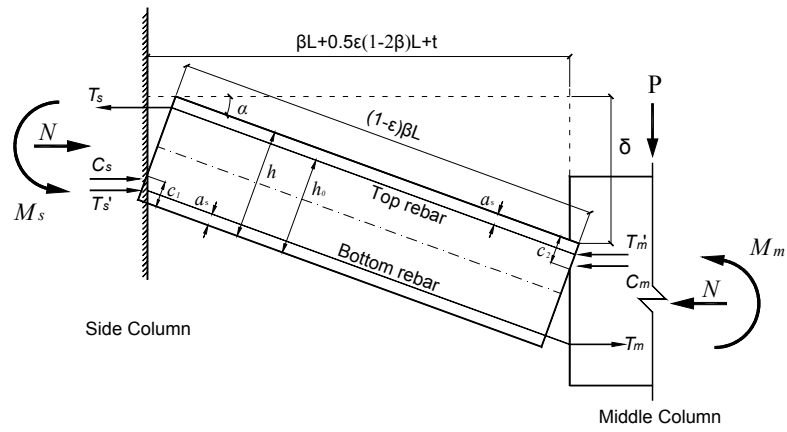
(b)

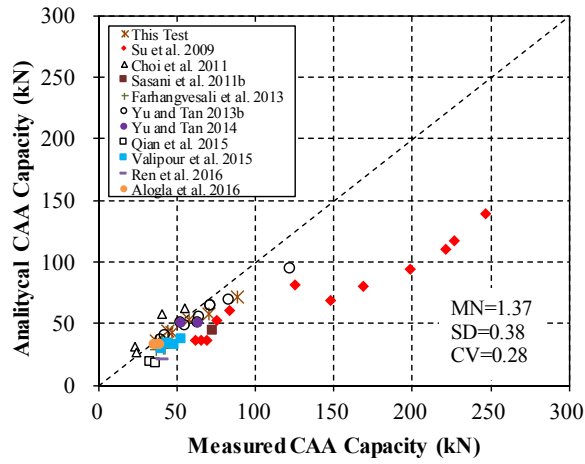


(a)

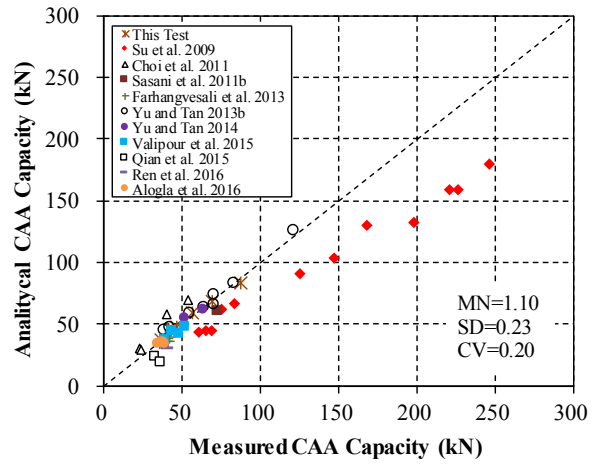


(b)

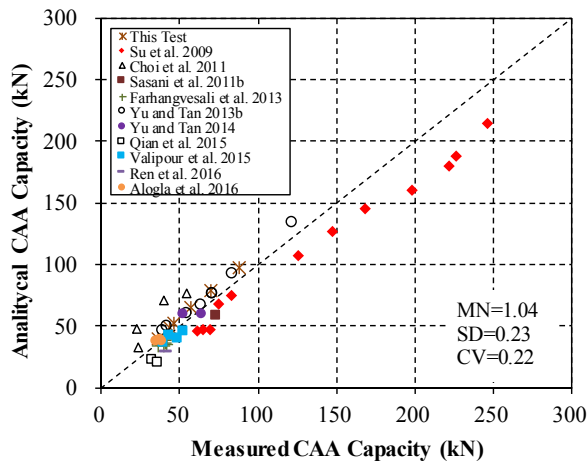




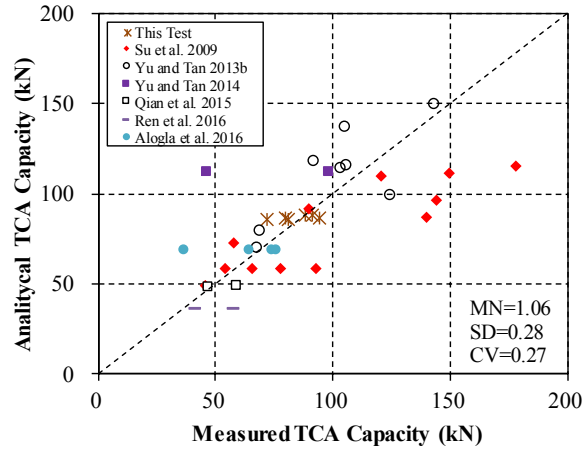
(a)



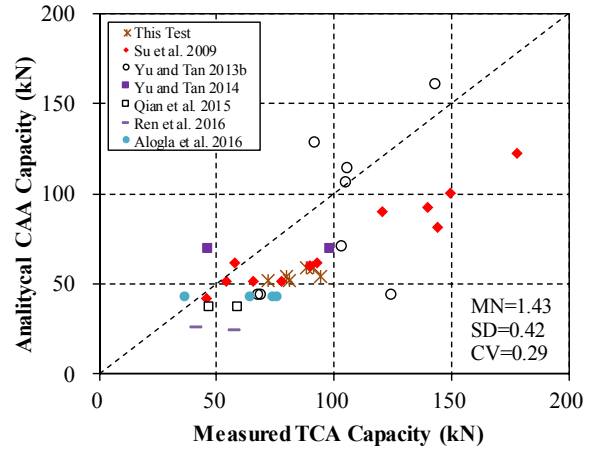
(b)



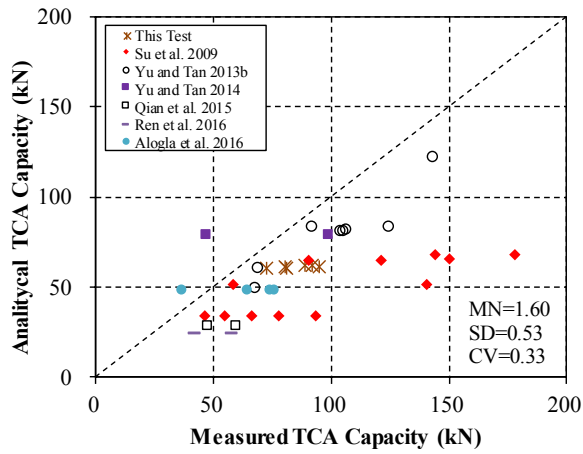
(c)



(a)



(b)



(c)